



Direct simulation of flow-boiling crisis and its porous-metasurface control for very large dryout limit

Júlio Ferreira, Massoud Kaviany*

Department of Mechanical Engineering, University of Michigan, Ann Arbor, MI, 48109, United States



ARTICLE INFO

Article history:

Received 28 January 2022

Revised 9 May 2022

Accepted 17 May 2022

Keywords:

Flow boiling critical heat flux
Porous metasurface
Zuber pool boiling CHF unit cell
Critical wavelength
Wavelength modulation
Hydrodynamic instability
Kelvin-Helmholtz instability
Rayleigh-Taylor instability
Capillary-viscous limit
Superheat limit
Direct numerical simulation of flow boiling
Large eddy simulation of two-phase flow

ABSTRACT

The Zuber pool-boiling hydrodynamic instability theory establishes that the critical heat flux $q_{CHF,z}$ is based on rising surface vapor columns with liquid counterflow in a unit cell the of size of the critical wavelength λ_c determined by the Kelvin-Helmholtz and Rayleigh-Taylor interfacial instabilities. In the flow boiling, the forced velocity $u_{l,o}$ creates a leading-edge region complementing these phase-buoyant flows and breaking the periodicity of the Zuber unit cell. Here, with the direct numerical simulations (DNS), i.e., CFD-VOF-LES, of the Zuber unit cell for saturated water (one atm), the effect of $u_{l,o}$ on the hydrodynamic dryout $q_{CHF,h}$ is examined. The results show that the upstream liquid flow penetrates the boiling region, forming surface liquid tracks meandering between the vapor columns, and upon $q_{CHF,h}$ these tracks become unstable causing surface dryout. For $u_{l,o}$ as small as 5 cm/s, the axial liquid inertia deflects the vapor track and establishes the surface liquid track, raising $q_{CHF,h}$ noticeably over $q_{CHF,z}$ and this is in good agreement with the available experiments. From the available theories, DNS-results and dimensional analysis, a relation is found between $u_{l,o}$ and λ_c establishing the wavelength modulation enhancement of the $q_{CHF,h}$ by increasing $u_{l,o}$ which decreases λ_c . In this new relation $q_{CHF,h}$ is proportional to $u_{l,o}^{1/6}$. The limit on this modulation enhancement is the capillarity limit $q_{CHF,c} = 3.3 \text{ MW/m}^2$ compared to $q_{CHF,z} = 1.1 \text{ MW/m}^2$.

Next, the DNS results show that anisotropic arrangement of the vapor sites stabilizes the surface liquid track, thus increasing the $q_{CHF,h}$. This geometric control of the vapor sites is achieved with a 3-D perforated porous coating, e.g., the flow-boiling canopy wick (FBCW). This geometric-modulated CHF enhancement is much larger than the wavelength-modulation enhancement and its vapor shear instability limit is overcome with the use of levees (geometric confinement) allowing for $q > 10 \text{ MW/m}^2$. However, the FBCW has an internal capillary-viscous limit $q_{CHF,c-v}$ (about 5.2 MW/m^2 using sintered-powder wick) which favors small λ_c and currently is the bottleneck for achieving extremely large $q_{CHF,h}$ (which favors large λ_c).

© 2022 Elsevier Ltd. All rights reserved.

1. Introduction

In boiling crises, the competition between the liquid supply to the heated surface and the escaping generated vapor results in local surface dryout and this two-phase hydrodynamics has been the subject of theoretical and experimental studies and reviews [1–3]. In recent years, in particular as related to the thermal management of high heat flux devices, the control and enhancement of the dryout limit (critical heat flux, CHF) has brought renewed interest in understanding the boiling crises. In addition, advances in the computational two-phase flows [4,5] and turbulence modeling

[6–8] have allowed for the direct numerical simulations (DNS) and closer examination of the assumptions applied in the theoretical treatments.

The Zuber two-phase hydrodynamic instability theory of saturated pool boiling postulates that the CHF phenomenon is triggered by a combination of the Kelvin-Helmholtz and the Rayleigh-Taylor instabilities [9] and this was later expanded in [10,11]. Recently, the pool boiling CHF mechanism was simulated numerically (Lattice-Boltzmann Method), providing physical insights on the triggering mechanism for the boiling crisis [12] and the roles of surface wettability in reducing the surface superheat [13] and vapor recoiling in the formation of hot spots [14]. In saturated flow boiling, the inertia of the forced flow increases the CHF above the pool boiling limit and comprehensive reviews on the existing mechanistic CHF models are given in [15,16]. Among the

* Corresponding author.

E-mail address: kaviany@umich.edu (M. Kaviany).

Nomenclature

A	area (m ²)
Bo_L	Bond number, $\frac{(\rho_l - \rho_g)gL^2}{\sigma}$
C	inertial coefficient
c_p	heat capacity (J/kg-K)
D, d	diameter (m)
EO_L	Eötvös number, $\frac{(\rho_l - \rho_g)gL^2}{\sigma}$
Fr_L	Froude number, $\left[\frac{\rho_l u_{l,o}^2}{g(\rho_l - \rho_g)L} \right]^{1/2}$
G/A	thermal conductance [K/(W/m ²)]
g	gravity (m/s ²)
H, h	height (m)
Δh_{lg}	heat of evaporation (kJ/kg)
K	permeability (m ²)
k	thermal conductivity (W/m-K)
L, l	length (m)
M	dynamic pressure ratio, $\frac{\rho_g u_g^2}{\rho_l u_l^2}$
Ma_g	Mach number, $\frac{u_{g,o}}{u_a}$
p	pressure (Pa)
P	first velocity gradient invariant (1/s)
Q	heat flow rate (W), second velocity gradient invariant (1/s ²)
q	heat flux (W/m ²)
R	curvature radius (m), third velocity gradient invariant (1/s ³)
Re_L	Reynolds number, $\frac{\rho_l u_l L}{\mu_f}$
S	symmetric part of strain rate tensor (1/s)
t	time (s)
T	temperature (K)
\mathbf{u}	velocity vector (m/s)
u	axial velocity (m/s)
u_a	speed of sound (m/s)
v	lateral velocity (m/s)
V	volume (m ³)
w	perpendicular velocity (m/s)
W, w	width (m)
We_L	Weber number, $\frac{\rho_l u_{l,o}^2 L}{\sigma}$
x	axial position (m)
y	lateral position (m)
z	perpendicular position (m)
<i>Greek symbols</i>	
α	void fraction
δ	liquid thickness (m), interfacial perturbation
ϵ	porosity
κ	wavenumber (1/m)
λ	length scale (m)
μ	dynamic viscosity (Pa-s)
ν	kinematic viscosity (m ² /s)
ρ	density (kg/m ³)
σ	surface tension (N/m)
ω	vorticity (1/s)
Ω	antisymmetric part of strain rate tensor (1/s)
<i>Subscripts</i>	
c	capillary, critical
ca	canopy
ch	channel, choking
CHF	critical heat flux
$c - v$	capillary-viscous
e	evaporator

f	fluid
g	gas/vapor
h	hydrodynamic
i	index
j	index
k	index
K	Kolmogorov
KH	Kelvin-Helmholtz
l	liquid
lg	liquid-gas phase change
max	maximum
n	normal
o	outlet
p	particle, post
per	perforation
ps	plain surface
RT	Rayleigh-Taylor
s	surface
sh	superheat
Z	Zuber
<i>Others</i>	
$-$	temporal average
\sim	filtered
$'$	perturbation/fluctuation
$\langle \rangle$	spatial average
$*$	dimensionless

flow-boiling CHF models is the interfacial lift-off model, which combines a separated two-phase model with the Kelvin-Helmholtz and the Rayleigh-Taylor interfacial instabilities triggering the crisis [17–19] with good agreement between the predictions and experiments for rather narrow channels.

Although the bubble nucleation sites and bubble dynamics are stochastic, the Zuber theory of boiling crises and its extensions are based on two-phase unit cells, with periodic arrangement of the vapor columns. This periodicity (multiple symmetry) is suitable to the DNS of the boiling crises. High-fidelity simulations have been applied to different aspects of the pool and flow boiling phenomena (e.g., cavity activation, bubble growth cycle) [5,20], however, there are few studies of the flow boiling CHF. In [21,22], a model is proposed identifying CHF based on the local liquid film thickness compared with the amplitude of the interfacial waves in microchannels and using a separated flow model to resolve the flow field. In [23], a full 3-D CFD solver resolves the flow including mass transfer mechanisms, and the evaporation/condensation for different microchannel geometries, although before the CHF.

Using the unit-cell based DNS, in addition to verifying the theoretical predictions of the flow boiling crises, allows for modulation of the vapor column sites and explores the enhancement of the hydrodynamic CHF through this control. These modulated vapor sites are created using a porous metasurface [24], and this is explored with 3-D capillary structures such as the flow-boiling canopy wick [25–27]. However, the porous metasurface has an internal capillary viscous limit which may not allow reaching the higher modulated hydrodynamic limit.

Here, we review the unit-cell based, hydrodynamic instability theories of the pool and flow boiling (and their relations) and use them as the bases for relating the heat flux dryout limit to the vapor-site configuration. We use the DNS results to verify the theoretical predictions and to explore the hydrodynamic CHF enhancements by vapor-site modulation. Snapshots of phase distribution are used to monitor time variations of the liquid track width in the leading-edge close to the heated surface and identify its eventual dryout. Three hydrodynamic-limit regimes are defined, the

wavelength, the geometric, and the geometric-confined modulation regimes, and their boundaries are explored analytically using first principles. The related porous metasurfaces allowing for the modulations of the vapor sites and liquid supply, and the capillary-viscous limit are also treated. The quantitative results are for saturated water at one atm.

2. Boiling hydrodynamic instability theories

2.1. Zuber pool boiling CHF theory and unit cell

Initially separated two-phase flow has interfacial instabilities associated with it when there is relative motion between the phases [28]. The instabilities depend on the flow condition and can heavily impact the heat and mass transfer [29]. The linear stability analysis considers the interface between liquid and vapor (gas) to be planar and horizontal with the phases moving with axial velocities u_g and u_l . The derivation is summarized in Appendix A with details available in [29] and [30]. When the less dense phase (gas) is on top, the system is initially stable. The Kelvin-Helmholtz (K-H) instability arises when the relative velocity is larger than a critical value $|u_g - u_l| = u_c$. The corresponding K-H critical wavelength is

$$\lambda_{KH} = \lambda_c = 2\pi \left[\frac{\sigma}{g(\rho_l - \rho_g)} \right]^{1/2}. \quad (1)$$

The viscous effects are considered in [31].

When the more dense phase is on top, the Rayleigh-Taylor (R-T) instability arises with the critical wavelength (the most dangerous wavelength)

$$\lambda_{RT,d} = 3^{1/2} 2\pi \left[\frac{\sigma}{g(\rho_l - \rho_g)} \right]^{1/2} = 3^{1/2} \lambda_c. \quad (2)$$

So, the K-H and R-T critical wavelengths are related. The most dangerous R-T 3-D waveforms are arranged in a square lattice with each unit-cell side equal to the 2-D wavelength of Eq. (2) [29]. Equations (1) and (2) can be expressed with the Bond (or Eötvös) number (would become equal to 2π and $3^{1/2} 2\pi$), which is the ratio of buoyancy and surface tension forces

$$Bo_\lambda = \frac{g(\rho_l - \rho_g)\lambda_c^2}{\sigma} = \frac{We_\lambda}{Fr_\lambda^2}, \quad (3)$$

where the Froude and Weber numbers are a ratio of the inertial and gravity forces and a ratio of the inertial and surface tension forces, respectively

$$Fr_\lambda = \left[\frac{\rho_l u_{l,o}^2}{g(\rho_l - \rho_g)\lambda_c} \right]^{1/2}; \quad We_\lambda = \frac{\rho_l u_{l,o}^2 \lambda_c}{\sigma}. \quad (4)$$

The capillary length l_c is defined by the Bond number of unity, $Bo_\lambda = 1$, and signifies requiring an extra external force to keep the liquid and vapor phases separate

$$l_c = \left[\frac{\sigma}{(\rho_l - \rho_g)g} \right]^{1/2}. \quad (5)$$

For saturated water it is $l_c = 2.5$ mm. The K-H and R-T wavelengths are proportional to the capillary length.

Different pool-boiling critical heat flux (CHF) mechanisms are summarized in [29]. The Helmholtz instability mechanism states that the generated bubbles create unstable columnar vertical liquid-vapor interface and the CHF occurs when these columns impede the counterflow of liquid, ceasing the liquid supply. Zuber [9] adopted this mechanism as a basis for his theory for a flat plate.

As shown in Fig. 1, the vapor columns are arranged in a square array with side $\lambda_c = \lambda_{RT,d}$ from Eq. (2), and column diameter $d_g =$

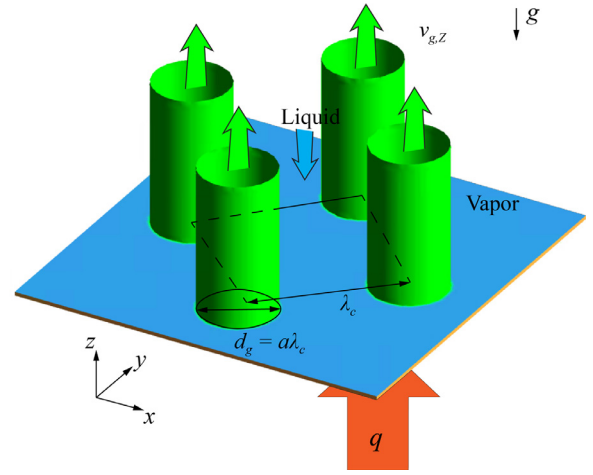


Fig. 1. Spatial distribution of vapor columns, with counter flowing liquid, on a horizontal flat plate in the Zuber critical heat flux model. This is the Zuber unit cell.

$a\lambda_c$, where $a = 1/2$. The square arrangement proposed by Zuber was later confirmed by Sernas et al. [32]. The CHF is then calculated as the heat removed from this rising vapor columns

$$q_{CHF} = \rho_g v_{g,z} \Delta h_{lg} \left(\frac{A_g}{A} \right)_z, \quad (6)$$

and the vapor velocity is found from K-H wavelength

$$v_{g,z} = \left(\frac{2\pi\sigma}{\lambda_{KH}\rho_g} \right)^{1/2}, \quad (7)$$

with the area ratio

$$\left(\frac{A_g}{A} \right)_z = \frac{\pi a^2 \lambda_c^2}{4\lambda_c^2}. \quad (8)$$

Substituting this velocity and area ratio into Eq. (6) results in the pool-boiling CHF

$$q_{CHF} = \rho_g \Delta h_{lg} \left(\frac{2\pi^3 a^4 \sigma}{\lambda_{KH} \rho_g} \right)^{1/2}, \quad (9)$$

with $\lambda_{KH} = \lambda_{RT,d} = \pi d_g$. Substituting this into Eq. (6) we find the Zuber CHF

$$q_{CHF,Z} = \frac{\pi}{24} \rho_g \Delta h_{lg} \left[\frac{\sigma(\rho_l - \rho_g)g}{\rho_g^2} \right]^{1/4}. \quad (10)$$

The wavelength adopted by Zuber corresponds to a Bond number $Bo_\lambda = 81$ and for saturated water at one atm, $q_{CHF,Z} = 1.1$ MW/m².

When it is possible to modulate the critical wavelength, as in [33] using a porous metasurface, the pool-boiling hydrodynamic CHF can be enhanced according to

$$q_{CHF,h} = \frac{\pi}{8} \Delta h_{lg} \left(\frac{\sigma \rho_g}{\lambda_c} \right)^{1/2}, \quad (11)$$

where $\lambda_c \leq \lambda_{RT,d}$ is the modulated wavelength. The smaller wavelength corresponds to smaller vapor columns, allowing for a larger vapor velocity when the K-H instability is triggered. The $q_{CHF,h}$ enhancement achieved by the wavelength modulation [discussed below and for pool boiling reported in [33]] is similar to the pool-boiling heater-size effect. Measured $q_{CHF,h}$ over the $q_{CHF,Z}$ have been reported using progressively smaller heaters, and the smallest heater size is considered to be the capillary length l_c [10,34].

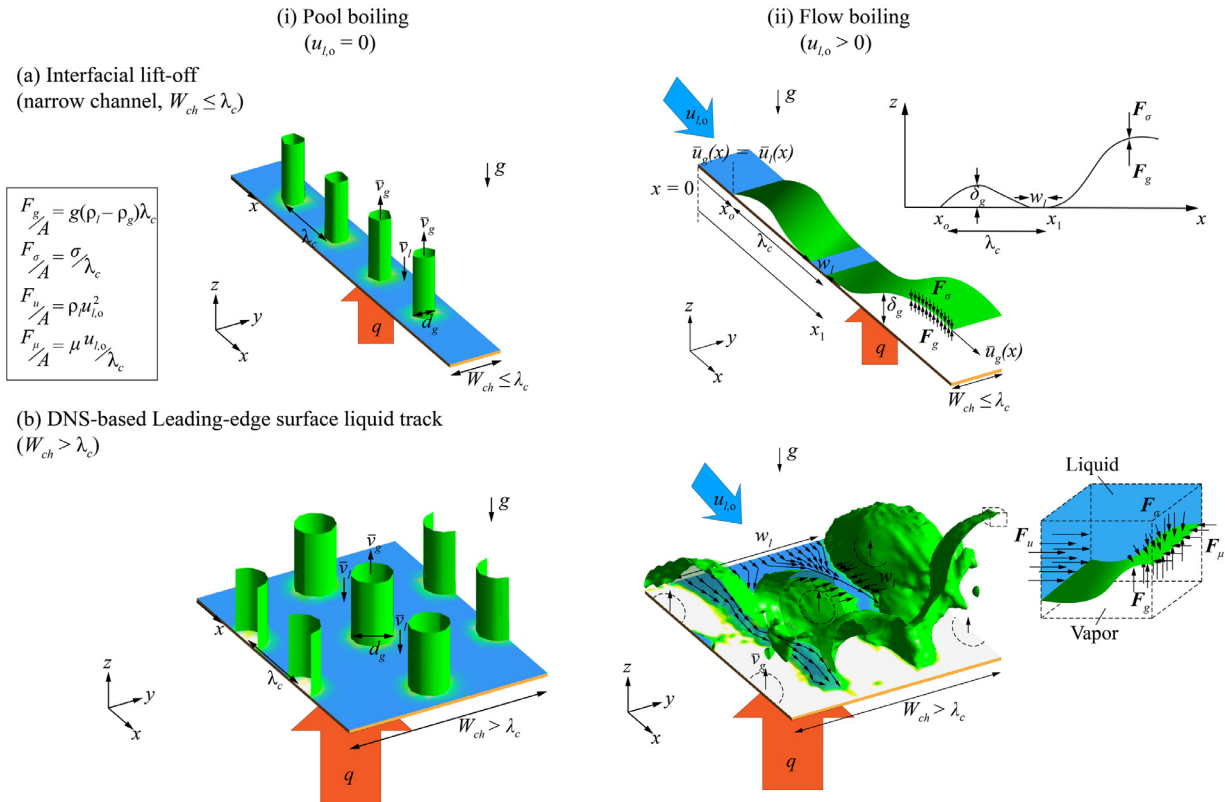


Fig. 2. Schematic representation of the liquid- and vapor-phase flow distribution in the transition from (i) pool boiling to (ii) flow boiling. (a) The 2-D interfacial lift-off model [17,18] (narrow channel). (b) 3-D DNS leading-edge surface liquid track model (wide channel). The models are based on the Zuber unit cell, and the dominant forces governing the CHF are the buoyancy, surface tension, inertial, and viscous.

2.2. Flow-boiling CHF theories

Differing from the pool boiling where the pressure gradient and the liquid momentum are in the gravity direction (z direction), the forced, axial inertial component of flow boiling breaks the symmetry of the counter, columnar two-phase flow of the Zuber unit cell shown in Fig. 1. The smallest axial flow fundamentally alters the boundary conditions.

Figure 2 illustrates this transition from pool to flow boiling, using the Zuber unit cell as the basis. Predicting the flow-boiling CHF has traditionally been done empirically. Although the correlations can provide useful results, they cannot be used outside the limits of their experiments, so we consider the first-principles, physical mechanisms triggering the CHF. The liquid supply mechanism in flow boiling is essential in defining the mechanisms responsible for the boiling crises. Four different mechanisms have been proposed and are widely accepted [15], namely, boundary-layer separation model [35], bubble-crowding model [36], sublayer dryout model [37], and interfacial lift-off model [17,18]. The last one states that the liquid is supplied from the top in the Zuber unit cell, however in a moving frame of reference [19]. This does not address the establishment of a leading-edge liquid track on the surface. This axial, forced surface liquid flow meanders around the vapor generated and escaping the surface. This fundamental change from the pool to the flow boiling leads to a jump in the critical heat flux with the smallest forced flow (verified with the DNS).

The interfacial lift-off model and the leading-edge, liquid track shear instability model, shown in Fig. 2, are discussed below.

The interfacial lift-off model [Fig. 2(a)(ii)] postulates that CHF occurs when the momentum of the generated vapor produced in small portions of the surface called the wetting fronts, responsible for providing liquid to the heated surface, overcomes the in-

terfacial pressure force, lifting the liquid away from the surface. In order to perform this balance, it employs three submodels. (i) A separated-flow model to determine the velocities and thicknesses of liquid and vapor in the channel. (ii) A hydrodynamic stability model which employs the results from the previous model to predict the interfacial shape and the critical wavelength of the vapor layer. (iii) A CHF trigger mechanism model, determined considering both the critical wavelength of the vapor and the Helmholtz wavelength in the wetting front [19]. This is identical to the Zuber formulation, where the surface is modelled as square unit cells containing vapor jets surrounded by liquid, with the jet diameter half the critical vapor wavelength from the second submodel, $d_g = \lambda_c/2$. The implementation of this model is discussed in [26,27].

The interfacial lift-off model is based on experimental measurements in a narrow channel ($W < \lambda_c$) with a single row of vapor jets. Figure 2(a) schematically illustrates the liquid and vapor flows in a narrow channel for pool and flow boiling conditions. The vapor expansion occupies the entire bottom portion of the channel, diverting the liquid upward and preventing the formation of a surface liquid track. Liquid supply is limited to the wetting fronts. The critical vapor wavelength λ_c corresponds to the vapor momentum lifting the interface, interrupting the liquid supply.

The axial velocities u_f ($f = g$ or l for vapor and liquid) are found from the 2-D separated-flow submodel and employed in the following submodel (hydrodynamic stability theory) to determine λ_c . The ascending vapor velocity and the liquid make-up velocity are found from the third submodel. In [19], the effect of the axial flow on the wetting fronts mimics the behavior of a moving wall generating columnar vapor jets, similar to the hydrodynamic instability present in Zuber analysis (the only difference being the moving frame of reference).

Similar to the pool boiling $q_{CHF,h}$ of Eq. (11), the interfacial lift-off theory [17–19] of flow-boiling dryout results in

$$q_{CHF,h} = \rho_g \Delta h_{lg} \frac{\pi}{8} \left(\frac{\sigma}{\lambda_c} \right)^{1/2} \left[\frac{\left(\frac{\rho_l + \rho_g}{\rho_l \rho_g} \right)^{1/2}}{1 + \frac{\rho_g}{\rho_l} \frac{\pi}{(16-\pi)}} \right], \quad (12)$$

where λ_c is found from the 2-D separated flow model and interfacial instability submodels [19]

$$\lambda_c = 2\pi \left[\frac{\rho'_l \rho'_g (u_g - u_l)^2}{2\sigma (\rho'_l + \rho'_g)} + \left\{ \left[\frac{\rho'_l \rho'_g (u_g - u_l)^2}{2\sigma (\rho'_l + \rho'_g)} \right]^2 + \frac{(\rho_l - \rho_g)g \cos(\phi)}{\sigma} \right\}^{1/2} \right]^{-1}, \quad (13)$$

where $\rho'_f = \rho_f \tanh^{-1}(\kappa H_f)$ is the modified phase density, H_f is the height occupied by the phase. The liquid and vapor phase velocities are calculated as

$$u_g = \frac{q_x}{\rho_g \delta (c_{p,l} \Delta T_{sub} + \Delta h_{lg})}, \quad (14)$$

$$u_l = \frac{u_{l,o} H}{H - \delta} - \frac{q_x}{\rho_l (H - \delta) (c_{p,l} \Delta T_{sub} + \Delta h_{lg})}, \quad (15)$$

where δ is the thickness of the vapor layer, from the separated flow model. The last term on the right of Eq. (12) is from the ascending vapor velocity and is related to the Helmholtz instability

$$v_{g,H} - v_{l,H} = \left(\frac{2\pi\sigma}{\lambda_H} \right)^{1/2} \left(\frac{\rho_l + \rho_g}{\rho_l \rho_g} \right)^{1/2}. \quad (16)$$

The continuity equation gives

$$v_{l,H} = \frac{\rho_g}{\rho_l} \left(\frac{\pi}{16 - \pi} \right) v_{g,H}. \quad (17)$$

The relationship between $q_{CHF,h}$ and the critical interfacial wavelength given in Eq. (12) for flow boiling in the interfacial lift-off model is functionally identical to Eq. (11), derived in [33] for pool boiling. Both express how $q_{CHF,h}$ can be modulated by λ_c and we will later discuss the control of λ_c with metasurfaces. Equation (11) was derived from the momentum balance of vapor emerging from the surface with a modified wavelength λ_c .

This wavelength modulation, achieved experimentally through porous metasurface with a periodic structural modulation of length λ_c supersedes the dependence only on the thermophysical properties given by the Rayleigh-Taylor wavelength, Eq. (3). This allows for the CHF enhancement beyond the Zuber limit for plain surface [33].

The interfacial lift-off theory identifies a similar dependency of the $q_{CHF,h}$ on the interfacial wavelength, obtained from the stability analysis of the 2-D two-phase flow using the separated flow model. The forced flow $u_{l,o}$ alters the characteristic wavelength λ_c , enhancing the $q_{CHF,h}$ similar to that achieved by λ_c modulation in pool boiling [33].

Equations (11) and (12) have identical λ_c dependence as shown in Fig. 3. In [33] a non-uniform porous coating was used with pentane as the fluid to modulate the λ_c and their experimental results (adjusted for water properties) are shown in Fig. 3, with good agreement to Eq. (11).

While Fig. 3 shows the flow boiling $q_{CHF,h}$ is equivalent to the surface wavelength modulation of pool boiling, we expect the anisotropic liquid inertia $u_{l,o}$ to alter the dryout crisis differently, and here we suggest a leading-edge surface liquid track instability guided by direct numerical simulation results. In Fig. 2(b),

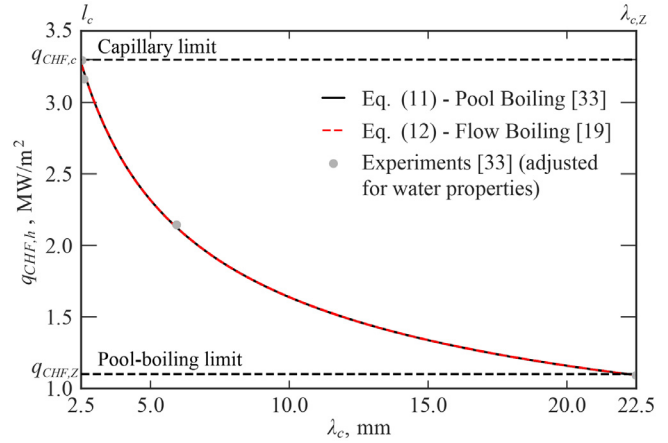


Fig. 3. Wavelength modulation of pool and flow-boiling dryout heat flux based on the Zuber unit-cell model. The pool-boiling results [33] are given by Eq. (11) and the flow-boiling interfacial lift-off theory results [17,18] are given by Eq. (12), and they are identical. The water-adjusted pool-boiling experimental results of [33] using a modulated porous coating are also shown.

this transition of the two-phase flow and distribution from the pool (i) to flow boiling (ii), under a wide-channel ($W_{ch} > \lambda_c$) treatment is rendered and fundamental forces outlined. The Zuber vapor columns of pool boiling are deflected in the flow direction, while a surface liquid track is formed in the leading-edge region and meanders around the vapor columns. This surface liquid track provides the axial liquid supply to the heated surface. This contrasts with the liquid supply in the interfacial lift-off theory with the submodel based on a narrow channel, where the liquid supply is from the top at the wetting fronts, triggering a Rayleigh-Taylor instability (liquid on top of vapor).

The two-phase flow rendered in Fig. 2(b)(ii) is hydrodynamically stable, with the surface liquid track formed in the leading-edge region beneath the vapor domain. As the vapor accelerates downstream, however, the interface relative velocity reaches a critical value, triggering the Kelvin-Helmholtz instability. This mechanism is dubbed the leading-edge surface liquid track instability and proposes the dryout is reached when the vapor shear causes the surface liquid track to shear break with the K-H instability downstream. The wide-channel condition $W_{ch} > \lambda_c$ allows for the lateral periodic treatment and formation of the liquid track, fundamentally altering the dryout mechanism. This is guided by direct numerical simulation of flow boiling using the Zuber unit cell as the basis, and existing experimental results.

3. Direct numerical simulations (DNS)

Figure 2 (b)(ii) renders the computational domain used in the direct numerical simulations (DNS) of flow-boiling and its crisis (surface dryout). The inlet liquid velocity $u_{l,o}$ is prescribed upstream, on the heated metasurface ($z = 0$) the vapor and liquid flows are prescribed for a given heat flux, lateral ($x - z$ plane) periodicity is used, shear-free top surface ($z = H_{ch}$), and continuous flow condition are used at the outlet downstream. Saturated water (one atm) is assumed. The related two-phase fluid mechanics (transient, 3-D Navier-Stokes equations) are solved numerically using ANSYS Fluent [38]. The treatment of turbulence is with Large Eddy Simulations. The unit-cell geometric parameters are related to heat flux according to Eq. (11), which is for pool boiling, however this critical heat flux depends on forced flow velocity $u_{l,o}$. The computational domain contains two axial and two lateral unit cells, with lateral periodicity. A leading and a trailing-edge region are added for more realistic upstream and downstream flow

Table 1
CFD condition and dimensionless numbers for different velocity regimes in the wavelength modulation regime.

Velocity regime	q , MW/m ²	$u_{l,o}$, m/s	λ_c , mm	Re_l	Re_g	Fr_λ	We_λ	Bo_λ	Ma_g	M
Low	1.35	0.05–0.25	17.7	3×10^3 – 15×10^3	5.7×10^3	0.1–0.6	0.7–18	50	0.01	0.45
Moderate	1.75	0.25–1	9.4	7.9×10^3 – 32×10^3	3.9×10^3	0.8–3.3	9.6–153	14	0.02	0.04–0.75
High	3	1–3	2.98	10×10^3 – 30×10^3	2.1×10^3	5.8–17.5	49–439	1.4	0.03	0.015–0.14

conditions. The vapor-column metasurface velocity and countering liquid flow are related to heat flux through

$$v_{g,o} = \frac{qA}{\rho_g \Delta h_{lg} A_g}; v_{l,o} = \frac{qA}{\rho_l \Delta h_{lg} (A - A_g)}, \quad (18)$$

where A is the unit-cell heated surface area and A_g the vapor column area, shown in Fig. 2(b). As an example, for saturated water at one atm and $q = 1.75$ MW/m², $v_{g,o} = 8.84$ m/s and $v_{l,o} = 0.95$ mm/s. As expected, the vapor velocity is about four orders-of-magnitude larger than the liquid.

An important distinction is that, in the channel, it is assumed that the two-phase flow is under saturated liquid-vapor condition (no evaporation or condensation), and the predicted results are compared with the saturation boiling experiments. No phase change is included in the two-phase flow, therefore empirical models for evaporation and condensation are not used. For the case of a plain surface, discussed in Section 4, the evaporation and the return of liquid to the surface are based on the Zuber unit cell model/theory as surface boundary conditions under saturated liquid-vapor condition. For the porous metasurfaces, discussed in Section 6, the vapor generation occurs in the evaporator layer wick of the FBCW, where the liquid is supplied to the evaporator layer through the porous posts which in turn are irrigated by the porous and perforated canopy. The liquid-film evaporation in the evaporator layer is modeled with one-dimensional heat conduction and the liquid film surface is assumed to be at the saturation temperature. So, the superheat is within the monolayer wick which is under local thermal equilibrium between the solid and liquid phase and the vapor is also at the saturated temperature (not superheated).

3.1. Dimensionless numbers

The liquid and vapor inertial forces are scaled with their respective viscosities in the Reynolds number for the liquid and vapor phases. As mentioned earlier, the role of the liquid-vapor interfacial tension is presented by the Weber number using the liquid inertia. For the role of gravity (buoyancy), the Froude number using the liquid inertia is used in Eq. (4). The compressibility limit of the vapor is addressed with the Mach number using the vapor speed of sound (for Mach number smaller than 0.3, the compressibility effects are neglected). The Zuber unit-cell size presented by wavelength λ_c is used for the length scale. In addition to Eq. (4), the Reynolds numbers, Mach number [4], and vapor to liquid inertial ratio are defined as

$$Re_l = \frac{\rho_l u_{l,o} \lambda_c}{\mu_l}, Re_g = \frac{\rho_g v_{g,o} \lambda_c}{\mu_g},$$

$$Ma_{g,per} = \frac{v_{g,per}}{u_a}, M = \frac{\rho_g u_g^2}{\rho_l u_l^2}. \quad (19)$$

The range of these dimensionless numbers are summarized in Table 1 for the range of liquid velocity $u_{l,o}$, typical heat flux, and the Zuber unit-cell presented by wavelength λ_c .

3.2. Treatment of liquid-vapor interface: Volume of fluid (VOF) method

Due to its mass conservation characteristics, the VOF method is preferred over the level-set method, but authors have employed a

combination of both [39]. In the VOF treatment, a single continuity and momentum conservation equations are used with an additional equation for the phase identifier, i.e., the volume fraction α

$$\frac{\partial}{\partial t} (\alpha \rho_g) + \nabla \cdot (\alpha \rho_g \tilde{\mathbf{u}}_g) = 0. \quad (20)$$

The phasic properties are used for the VOF properties, for example

$$\rho_f = \alpha \rho_g + (1 - \alpha) \rho_l, \quad (21)$$

$$\mu_f = \alpha \mu_g + (1 - \alpha) \mu_l. \quad (22)$$

The simulation time step restriction is based on the convection term, namely the Courant-Friedrichs-Lewy (CFL) condition [40], which states that the Courant number should be less than 0.25

$$Co = \Delta t \left(\frac{\tilde{u}_f}{\Delta x} + \frac{\tilde{v}_f}{\Delta y} + \frac{\tilde{w}_f}{\Delta z} \right) \leq Co_{max}. \quad (23)$$

3.3. Large eddy simulation (LES)

For a more accurate calculation of the two-phase flow turbulence, especially the flow adjacent to the heated metasurface and the state of the surface liquid track, the CFD simulations were conducted using the LES [41]. In the LES, the large turbulent eddies are resolved directly, while the small (i.e., subgrid) eddies are modeled. The momentum and mass are transported mostly by the large eddies which are significantly affected by the geometry and boundary conditions, while the small eddies tend to be more isotropic, and the conventional turbulent models are more suited for their prediction.

A filter is applied to the Navier-Stokes equations, effectively cutting off eddies smaller than the grid size. This filtering is analogous to the finite volume discretization.

These filtered Navier-Stokes equations are

$$\frac{\partial \rho_f}{\partial t} + \frac{\partial}{\partial x_i} (\rho_f \tilde{u}_{f,i}) = 0, \quad (24)$$

$$\frac{\partial}{\partial t} (\rho_f \tilde{u}_{f,i}) + \frac{\partial}{\partial x_j} (\rho_f \tilde{u}_{f,i} \tilde{u}_{f,j}) = \frac{\partial \sigma_{ij}}{\partial x_j} - \frac{\partial \tilde{p}}{\partial x_j} - \frac{\partial \tau_{ij}}{\partial x_j}, \quad (25)$$

where σ_{ij} is the viscosity stress tensor component and τ_{ij} is the subgrid-scale stress component, described in Appendix B. The subgrid-scale resulting from the filtering operation requires modeling. As in Reynolds-averaged Navier-Stokes (RANS) equations, the Boussinesq hypothesis is employed and the stresses are [42]

$$\tau_{ij} - \frac{1}{3} \tau_{kk} \delta_{ij} = -2 \mu_{f,t} \tilde{S}_{ij}. \quad (26)$$

Alongside the void-fraction, the Q -criterion, a vortex identification method, also shows that vortices are limited to the vapor phase. The vorticity is

$$\omega = \nabla \times \mathbf{u}_f, \quad (27)$$

and its presentation requires the velocity gradient tensor invariants, P , Q , and R . These invariants are the coefficients of the cubic characteristic polynomial $\det(\nabla \mathbf{u}_f - \lambda \mathbf{I})$, i.e.,

$$\lambda^3 + P\lambda^2 + Q\lambda + R = 0, \quad (28)$$

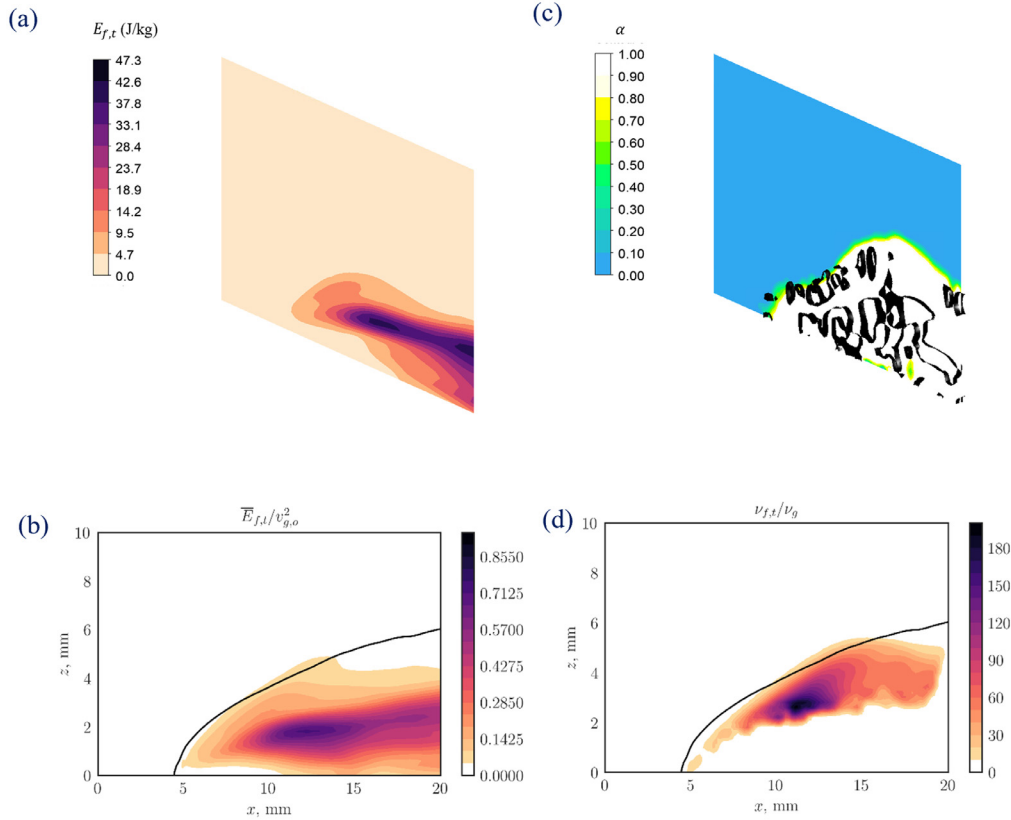


Fig. 4. (a) Predicted distribution of the instantaneous, constant interfacial shear-flow turbulent kinetic energy $\bar{E}_{f,t}$ contours in the axial midplane for plain surface for $q = 1.75 \text{ MW/m}^2$, $u_{l,o} = 0.5 \text{ m/s}$. (b) Contour of constant time-averaged turbulence kinetic energy $\bar{E}_{f,t}$. Instantaneous contours of constant (c) invariant $Q = 1 \text{ 1/s}^2$, and (d) eddy viscosity $\mu_{f,t}$. The results are for saturated water at one atm, and $y = 0$.

where $P = -S_{ij}$, $Q = \frac{p^2 - S_{ij}S_{ji} + \Omega_{ij}\Omega_{ji}}{2}$, and $R = \frac{-p^3 + 3pQ - S_{ij}S_{jk}S_{ki} - 3\Omega_{ij}\Omega_{jk}\Omega_{ki}}{2}$. For incompressible flows, the first invariant is $\bar{P} = 0$ (since $\nabla \cdot \mathbf{u}_f = 0$), so the so-called Q -criterion is derived based on the second invariant [43], and is

$$Q = \frac{1}{2} (\|\boldsymbol{\Omega}\|^2 - \|\mathbf{S}\|^2), \quad (29)$$

where \mathbf{S} is the symmetric part of the strain rate tensor and $\boldsymbol{\Omega}$ is its antisymmetric part (vorticity tensor). The Q -criterion states that $Q > 0$ represents a vortex. There are other methods for vortex identification available [44], however we use Eq. (29). Further discussions of the turbulence treatment is given in Appendix B.

Figure 4 (a) to (d) show the distributions in the axial midplane ($y = 0$) of the turbulence quantities for $q = 1.75 \text{ MW/m}^2$ and $u_{l,o} = 0.5 \text{ m/s}$. The black line denotes the liquid-vapor interface. Figure 4(a) and (b) show that the turbulence is generated at the liquid-vapor interface and it is noticeably more intense in the vapor phase, this is in agreement with recent studies of two-phase LES that show the occurrence of interface-generated turbulent eddies [45–47]. The peak in the turbulent kinetic energy $\bar{E}_{f,t}$ is in the vapor phase in the leading-edge region, where the incoming liquid flow is severely deflected and broken by the vapor columns. In this region, the vapor inertia overcomes the surface tension to enter the liquid channel flow. Near the liquid inlet, the relative liquid-vapor velocity is the largest, because the liquid has not yet accelerated and the vapor velocity has not changed from its large magnitude prescribed by the heat flux boundary condition, four-order-of-magnitude larger than the liquid.

Figure 4 (c) shows isosurface of the Q -criterion for $Q = 1 \text{ 1/s}^2$ superposed on the void fraction distribution in the axial midplane. All the vortical structures identified by the Q -criterion re-

main within the vapor phase. Vortical structures dissipate turbulent kinetic energy [45]. Similarly, the eddy viscosity distribution is shown in Fig. 4(d). It is calculated using Eq. (26), is proportional to the Reynolds stresses normalized by the mean strain rate. Its peak is observed just beneath the interface and is compatible with the distribution of the vortices (and the large gradient components) occurring mainly within the vapor phase. These analyses of the turbulent quantities were repeated for all CFD runs with similar trends found regarding the turbulent vortical structure and distribution.

3.4. Dryout limit from the DNS

The direct simulations are used to verify the CHF wavelength-modulation regime for the plain surface, while varying the liquid velocity $u_{l,o}$. We begin by choosing a CHF and finding λ_c according to Eq. (11). Several iterations are required to determine the relation between $u_{l,o}$ and $q_{CHF,h}$. In these iterations, either $u_{l,o}$ is varied while q is kept constant or vice-versa (and consequentially unit-cell is changed). The outcome is the $u_{l,o}$ corresponding to $q_{CHF,h}$ calculated using Eq. (11), which depends on the thermophysical properties and the Zuber unit cell, presented by the wavelength λ_c . So, the inlet velocity affects the λ_c , thus altering $q_{CHF,h}$.

So, for a given q , the λ_c is determined from Eq. (11) and for a plain surface geometry, simulations are conducted with this wavelength and progressively smaller $u_{l,o}$ to find the $u_{l,o}$ corresponding to the identified surface dryout (within the sensitivity of the practical $u_{l,o}$ or q steps in the simulation).

To determine dryout, the width of liquid track $\langle w_l \rangle$ in the simulated unit-cell based domain of the heated surface is used. Instantaneous as well as running-time average values are used. The

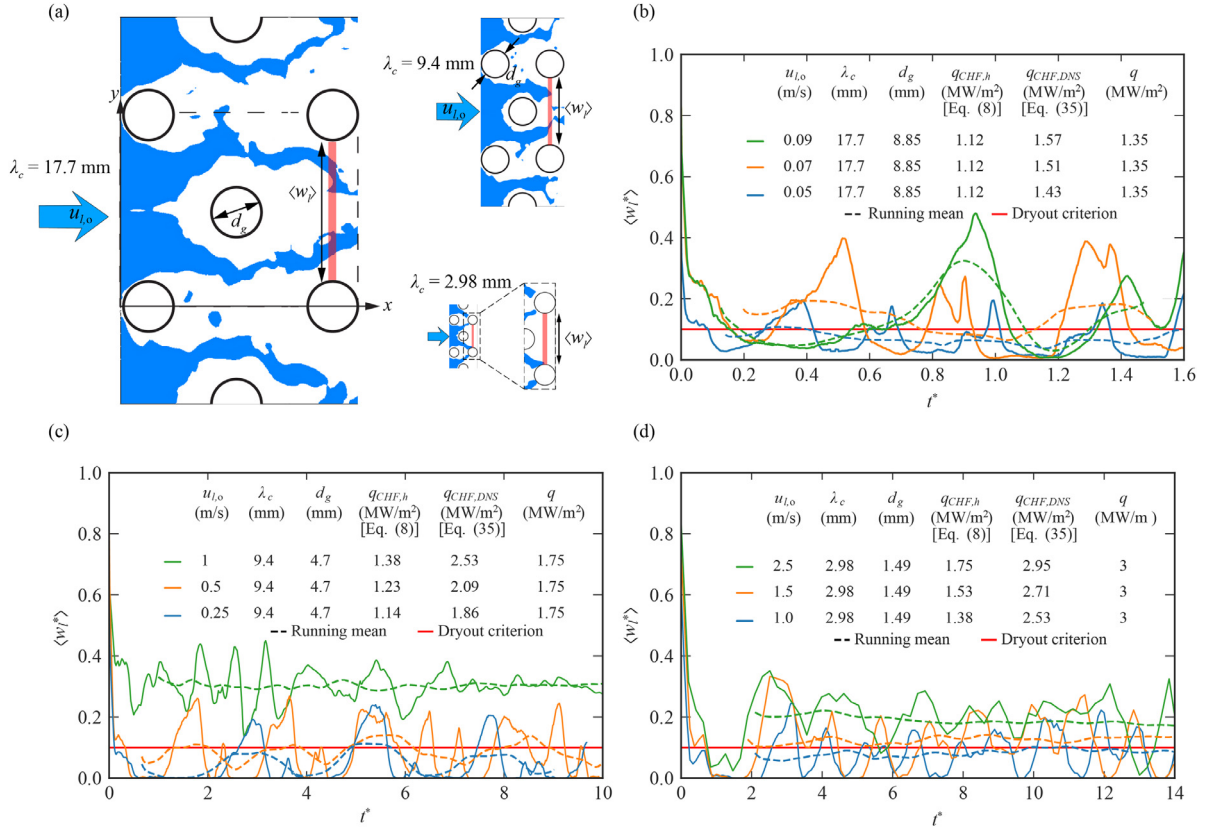


Fig. 5. (a) Snapshots showing the liquid track width (w_l) at the location marked by the red strip. Time variations of the normalized liquid track width for (b) $q = 1.35$ MW/m² and $u_{l,o} = 0.05, 0.07$ and 0.09 m/s, (c) $q = 1.75$ MW/m² and $u_{l,o} = 0.25, 0.5$ and 1.0 m/s, and (d) $q = 3$ MW/m² and $u_{l,o} = 1, 1.5$ and 2.5 m/s, respectively. The results are for saturated water at one atm. (For interpretation of the references to colour in this figure legend, the reader is referred to the web version of this article.)

phase distribution in the $x - y$ plane at elevation $z = 0.25$ mm is used to detect the liquid phase and a phase marker is used to measure this width. The liquid-phase volume with $\alpha < 0.5$ has a marker value of 1, while the vapor-phase is marked with a value of 0. The liquid track width is determined as the summation of the marked pixels, and presence of vapor reduces $\langle w_l \rangle$. The summation is done over a rectangular domain ($\Delta x \Delta y$) and is then normalized by the integral length of the liquid track which is $\Delta y = \lambda_c(3^{1/2} - 1/2)$ ($\Delta x = \Delta y/10$), as shown in Fig. 5(a), i.e.,

$$\langle w_l^* \rangle = \frac{1}{\Delta x} \sum_i^{\Delta x} \left(\frac{1}{\lambda_c(3^{1/2} - 1/2)} \sum_i^{\Delta y} f \right), \begin{cases} f = 0, & \alpha \geq 0.5 \\ f = 1, & \alpha < 0.5 \end{cases} \quad (30)$$

Figure 5(b) to (d) show the time variations of the instantaneous and running-time averaged dimensionless liquid track width. In order to account for the different velocities and wavelengths, a dimensionless time, normalized by the fluid transit time is used, i.e.,

$$t^* = \frac{t u_{l,o}}{\lambda_c} \quad (31)$$

The dashed lines denote the running-time average which is averaging over elapsed time t of n steps

$$\langle \bar{w}_l^* \rangle = \frac{1}{t} \sum_n \langle w_l^* \rangle \quad (32)$$

When the liquid supply was interrupted for a time period long enough to trigger the rapid rise in the surface superheat observed in the boiling crisis, dryout occurs. Here, this criterion for the dryout is when $\langle w_l^* \rangle < 0.1$. These are marked in Fig. 5(b) to (d).

Figure 5(a) defines the downstream location in the computational domain where the liquid track is evaluated for dryout or

lack of it. Figure 5(b) to (d) show the dimensionless-time variations of the dimensionless liquid track width $\langle w_l^* \rangle$, for different heat fluxes with progressively smaller inlet liquid velocities. In Fig. 5(b), the heat flux is $q = 1.35$ MW/m², corresponding to $\lambda_c = 17.7$ mm [Eq. (11)], and $u_{l,o} = 0.05, 0.07$ and 0.09 m/s. The running-time average from Eq. (32) is shown with broken lines. The surface dryout criterion of $\langle w_l^* \rangle \leq 0.1$, marked by the red horizontal line, appears to present the breakup/interruption of the liquid track. Based on this, the dryout is marked for $u_{l,o} = 0.05$ m/s, since the running mean is consistently below this dryout criterion. Figure 5(c) is for $q = 1.75$ MW/m², corresponding to $\lambda_c = 9.4$ mm, and $u_{l,o} = 0.25, 0.5$ and 1 m/s. Again, dryout is observed for the lowest velocity, i.e., 0.25 m/s. Figure 5(d) shows the liquid track width variations for $q = 3$ MW/m², corresponding to $\lambda_c = 2.98$ mm, and $u_{l,o} = 1, 1.5$ and 2.5 m/s. Dryout is identified to occur when the liquid velocity is $u_{l,o} = 1$ m/s.

The DNS allows for using Zuber pool-boiling surface unit-cell assumption and then adding the forced flow $u_{l,o}$. The case of $u_{l,o} = 0$ is not realized, but liquid velocities as small as 5 cm/s can be simulated without major computational time challenges. We will further discuss this in the next section.

Figure 6 shows the snapshots of the phase distributions for the nine flow-boiling conditions shown in Fig. 5(b) to (d). The liquid-vapor interface is green and the surface liquid track is blue.

3.5. Temporal and spatial resolution convergence

The finest grid size investigated was $\Delta x_i = 0.15$ mm. Increasingly coarser grid sizes were evaluated and the value of $\Delta x_i = 0.25$ mm was selected since it presented an error of 1.9% at a reasonable computational cost. Although at a reduced computational

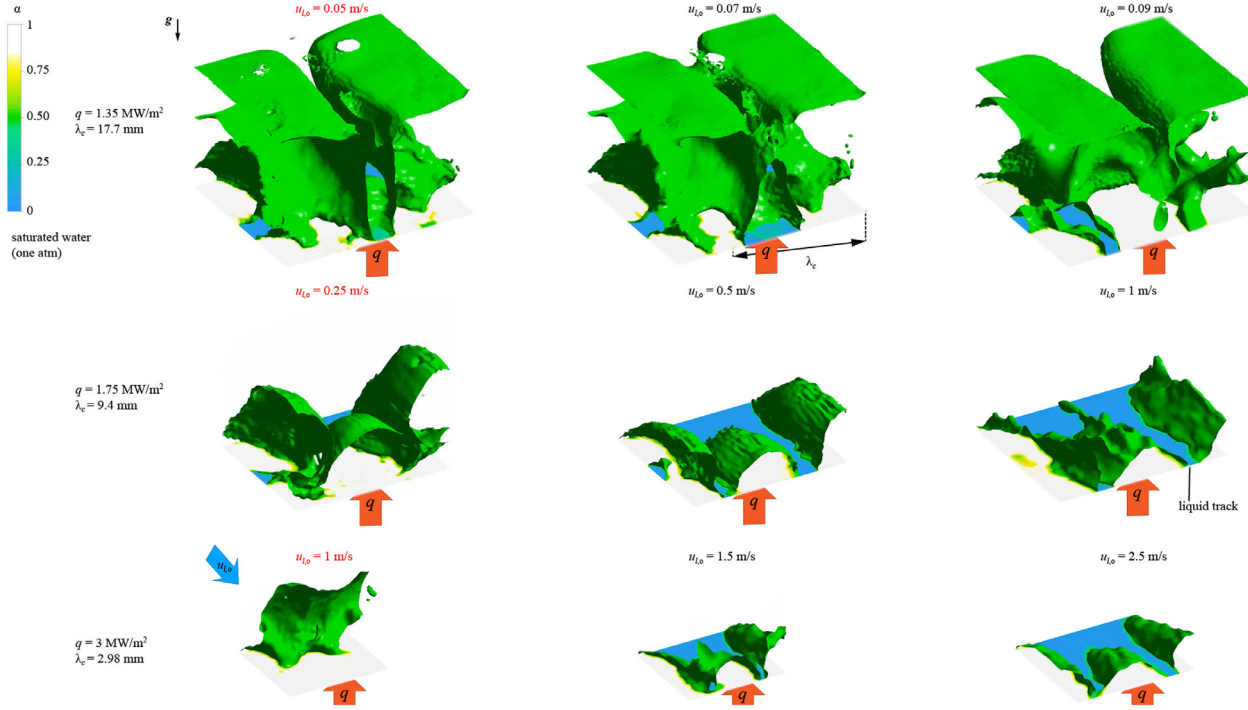


Fig. 6. Snapshots of phase distribution and the liquid track for the nine DNS conditions of Fig. 5, namely: $q = 1.35 \text{ MW/m}^2$ and $u_{l,o} = 0.05, 0.07$ and 0.09 m/s , $q = 1.75 \text{ MW/m}^2$ and $u_{l,o} = 0.25, 0.5$ and 1.0 m/s , and $q = 3 \text{ MW/m}^2$ and $u_{l,o} = 1, 1.5$ and 2.5 m/s , respectively. Velocities marked in red indicate cases for which dryout was observed. The results are for saturated water at one atm. The full video is available in the supplementary materials. (For interpretation of the references to colour in this figure legend, the reader is referred to the web version of this article.)

Table 2
Variation of running-time averaged dimensionless liquid track (Eq. (32)) for $q = 1.75 \text{ MW/m}^2$ and $u_{l,o} = 1 \text{ m/s}$.

Δx_i (mm)	$\langle \bar{w}_l^* \rangle$	$\frac{ \langle \bar{w}_l^* \rangle - \langle \bar{w}_l^* \rangle(\Delta x_i=0.15) }{\langle \bar{w}_l^* \rangle(\Delta x_i=0.15)}$ (%)
0.15	0.303	0.0
0.25	0.309	1.9
0.40	0.343	13.2
0.50	0.376	24.1

cost, coarser grid sizes ($\Delta x_i = 0.40$ and 0.50 mm) resulted in inaccurate measurements (error too high). As an example, Table 2 summarizes the variations of the running-time averaged liquid track $\langle \bar{w}_l^* \rangle$, defined by Eq. (32), with respect to progressively coarser grid size, for $q = 1.75 \text{ MW/m}^2$ and $u_{l,o} = 1 \text{ m/s}$ for saturated water at one atm.

The time step was selected to satisfy the CFL condition which, combined with the grid size, should result in $Co \leq 0.25$. The adopted time step is $\Delta t = 0.25 \mu\text{s}$.

4. Wavelength-modulation regime $q_{CHF,h}$ based on surface liquid track

In Fig. 3, it was suggested that using the Zuber model, the wavelength variation of $q_{CHF,h}$, i.e., its enhancement, is similarly achieved in pool and flow boiling. In pool boiling this has been achieved by non-uniform (3-D modulated with pitch λ_c) porous coating and in plain-surface flow boiling by the liquid velocity $u_{l,o}$. This is based on Zuber unit cell and surface vapor and liquid flow prescriptions. The support for this assumption/treatment is the expected tendency that under $u_{l,o} \rightarrow 0$, we should recover pool boiling. However, the slightest $u_{l,o}$ would break the streamwise symmetries and conditions. So, the relationship between λ_c and $u_{l,o}$ would address how the anisotropy is created by $u_{l,o}$ and here we

examine this as used in the interfacial lift-off submodel as it is found by the DNS.

In the lift-off submodel, Eq. (13) gives the dependency of the critical wavelength λ_c on the velocity of the liquid-phase u_l , given by Eq. (15). Equation (13) indicates that buoyancy and surface tension forces are balanced to determine the critical wavelength. At high velocities, when the gravity is negligible, i.e., $\frac{\rho_l' \rho_g' (u_g - u_l)^2}{2\sigma(\rho_l' + \rho_g')} \gg$

$$\left[\frac{(\rho_l - \rho_g)g \cos(\phi)}{\sigma} \right]^{1/2} = 400 \text{ 1/m}, \text{ or when the relative velocity } u_g - u_l \geq 6.37 \text{ m/s, this becomes}$$

$$\lambda_c = \frac{2\pi\sigma(\rho_l' + \rho_g')}{\rho_l' \rho_g' (u_g - u_l)^2} \approx \frac{2\pi\sigma}{\rho_g' (u_g - u_l)^2}, \quad (33)$$

suggesting a Weber number relationship, or dominance of the surface tension component.

In the interfacial lift-off submodel, the vapor momentum is determined by the balance between buoyancy and surface tension, Fig. 2(a)(ii), i.e., the Weber number and Froude number squared (which is the Bond number). This treatment, similar to that used by Zuber for pool boiling, does not include the liquid inertia, which further prevents the vapor from displacing the liquid. The complete derivation is made available in Appendix A as presented in [29,30].

For flow boiling, the contribution of the forced axial flow cannot be neglected, as in Fig. 2(b)(ii) the surface liquid supply depends on the axial flow. The forced liquid flow penetrates downstream and through the vapor columns, based on the modulated Zuber unit cell, ensuring the irrigation of the heated surface. This modulation is responsible for the $q_{CHF,h}$ enhancement over the $q_{CHF,Z}$ and is attributed to $u_{l,o}$, as shown in Fig. 3.

The surface vapor columns disturb the surface liquid track and this disturbance depends on the inertia of the forced liquid flow and the inertia of the escaping vapor columns, adjacent to the surface. Table 1 lists these liquid and vapor Reynolds number. So, when including these inertiae, in particular the effect of liquid

viscosity, which are not included in the K-H and R-T stability analysis, needs to be considered in the surface liquid track fluid mechanics. As outlined in Fig. 2(b)(ii) and with the snapshots shown in Fig. 6, it is the continuous surface liquid track that irrigates the heated surface, and its interruption leads to the flow-boiling dryout.

This effect can be included by multiplying the Bond number by the Reynolds number of the liquid phase. So here we proposed inclusion of the liquid inertia, which is also present in the DNS, and assume this product is a constant,

$$\frac{We_\lambda}{Fr_\lambda^2} Re_\lambda = Bo_\lambda Re_\lambda = \frac{g(\rho_l - \rho_g)\lambda_c^2}{\sigma} \frac{\rho_l u_{l,o}}{\mu_l} = C^2. \quad (34)$$

The constant C^2 is found from Table 1, and for high velocities, $C \approx 200$. This relation between the critical wavelength and the inlet velocity is of the form $\lambda_c \approx u_{l,o}^{-1/3}$. Rewriting Eq. (34) and replacing the wavelength from Eq. (11), we have

$$q_{CHF,h} = \frac{\pi}{8} \Delta h_{lg} (\sigma \rho_g)^{1/2} \left[\frac{g(\rho_l - \rho_g) \rho_l u_{l,o}}{C^2 \sigma \mu_l} \right]^{1/6}. \quad (35)$$

Using the capillary length l_c , the dimensionless $q_{CHF,h}$ becomes

$$\frac{q_{CHF,h}}{\rho_g^{1/6} \Delta h_{lg} [\sigma g(\rho_l - \rho_g)]^{1/4}} = \frac{\pi}{8C^{1/3}} Re_\lambda^{1/6}. \quad (36)$$

This is comparable to the dimensionless Zuber CHF, Eq. (9), i.e.,

$$\frac{\pi}{8C^{1/3}} \frac{u_{l,o,min}^{1/6}}{v_l^{1/6}} \left[\frac{\sigma}{g(\rho_l - \rho_g)} \right]^{1/12} = \frac{\pi}{24} \frac{\rho_g \Delta h_{lg} \left[\frac{\sigma(\rho_l - \rho_g)g}{\rho_g^2} \right]^{1/4}}{\rho_g^{1/6} \Delta h_{lg} [\sigma g(\rho_l - \rho_g)]^{1/4}}, \quad (37)$$

where $C = 200$.

Solving for the liquid inlet velocity, the minimum $u_{l,o}$ giving to $q_{CHF,Z}$, we find $u_{l,o,min} = C^2 \frac{v_l}{729l_c} = 6$ mm/s. Similarly, comparing Eq. (36) to the CHF for flow boiling given by Eq. (11), for $\lambda_c = l_c$, i.e., $q_{CHF,c}$ we have

$$\frac{\pi}{8C^{1/3}} \frac{u_{l,o,max}^{1/6}}{v_l^{1/6}} \left[\frac{\sigma}{g(\rho_l - \rho_g)} \right]^{1/12} = \frac{\pi}{8} \frac{\Delta h_{lg} (\sigma \rho_g)^{1/2} \left[\frac{g(\rho_l - \rho_g)}{\sigma} \right]^{1/12}}{\rho_g^{1/6} \Delta h_{lg} [\sigma g(\rho_l - \rho_g)]^{1/4}}, \quad (38)$$

solving once again for liquid the inlet velocity, corresponding to $q_{CHF,c}$ is $u_{l,o,max} = C^2 \frac{v_l}{l_c} = 5$ m/s.

Figure 7 (a) shows the variations of the $q_{CHF,h}$ and critical wavelength with respect to the inlet velocity for the interfacial lift-off and the surface liquid-track dryout models. The available experimental data for saturated water flow-boiling on plain surface CHF and wider channels ($We_{ch} > \lambda_c$) [48–51] are also shown. Pool boiling CHF data (corresponding to $u_{l,o} = 0$ m/s and $\lambda_c = \lambda_{c,Z}$) [52–54] are marked on the y axis. The error bars denote the CHF measurement uncertainty and the blue band depicts a 25% uncertainty in the value of the constant C in Eq. (34). The DNS results obtained according to the iterative process described in Section 3.4 are also shown. The three data points correspond to the lowest velocities ($u_{l,o} = 0.05, 0.25$ and 1 m/s) from Fig. 5(b) to (d), for $q_{CHF,h} = 1.35, 1.75$ and 3 MW/m², respectively. The $u_{l,o}^{1/6}$ relation correlates well the available data for the entire velocity range, presenting a smaller maximum absolute error than the interfacial lift-off results, denoted by the red line. Figure 7(b) uses log-log scale to show the low velocity results more clearly. Figure 7(c) show the variations of the critical wavelength with the liquid velocity from the lift-off and surface liquid-track, DNS results.

Both the high-velocity capillary limit, believed to be the upper limit of wavelength modulation enhancement, and the zero-velocity (pool-boiling) limit are also marked. Experiments with flow velocities smaller than 1 cm/s are rather scarce in the literature, so the minimum $u_{l,o}$ from Eq. (37) cannot be verified.

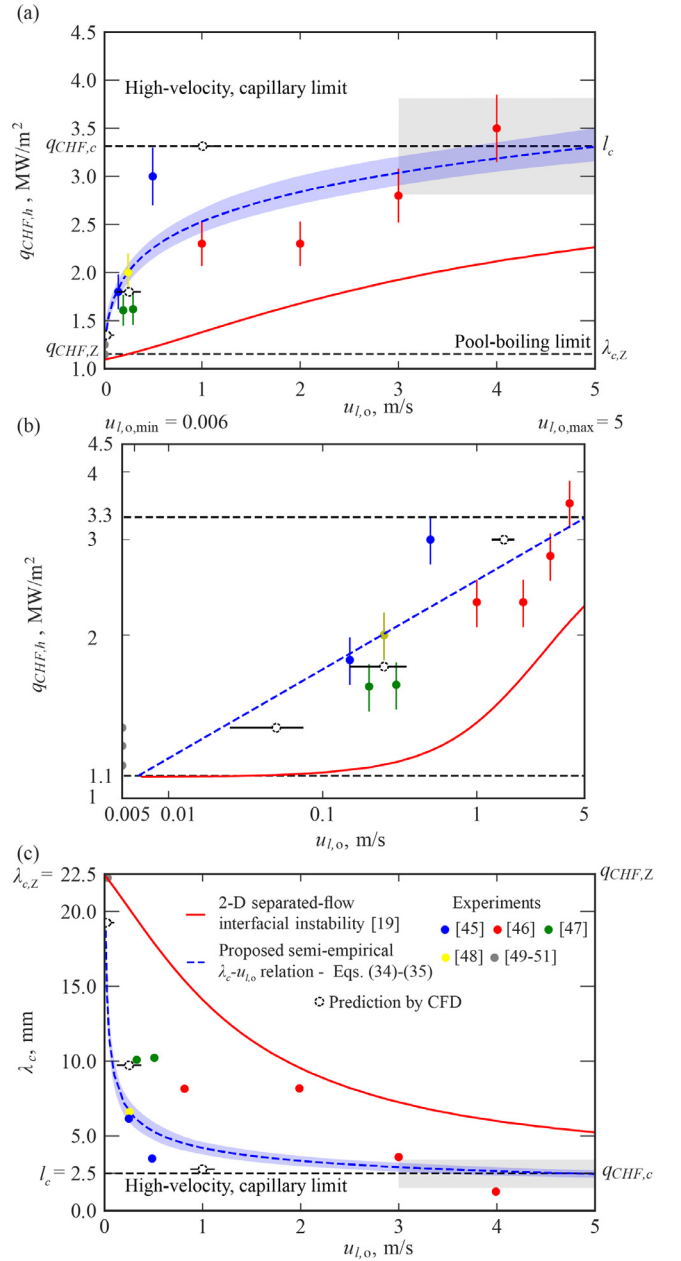


Fig. 7. Variations of hydrodynamic CHF with the inlet velocity for saturated water (1 atm) in (a) linear and (b) log-log scales. (c) Variations of the critical wavelength with the inlet velocity. The results are predictions from the interfacial lift-off and surface liquid-track models as well as the experimental and DNS results.

5. Vapor-site geometric-modulation regime $q_{CHF,h}$

In the hexagonal surface vapor-site arrangement, the liquid track meanders and this disturbs and can break its streamwise continuous surface coverage. In flow boiling the liquid supply may be exclusively from this axial flow, so the alignment of vapor sites may matter.

Figure 8 (a) renders these vapor escape sites (also referred to as surface perforations), following the Zuber unit-cell model, arranged in hexagonal (staggered) and square packing (inline, aligned with the flow direction). Figure 8(b) shows the time variations of the surface liquid track width $\langle w_l \rangle$ for $q = 1.75$ MW/m² and $u_{l,o} = 0.25$ m/s. Dryout is clearly observed for the staggered arrangement. The inline arrangement presents an increase over the staggered, but less so than the inline rectangular vapor inlets.

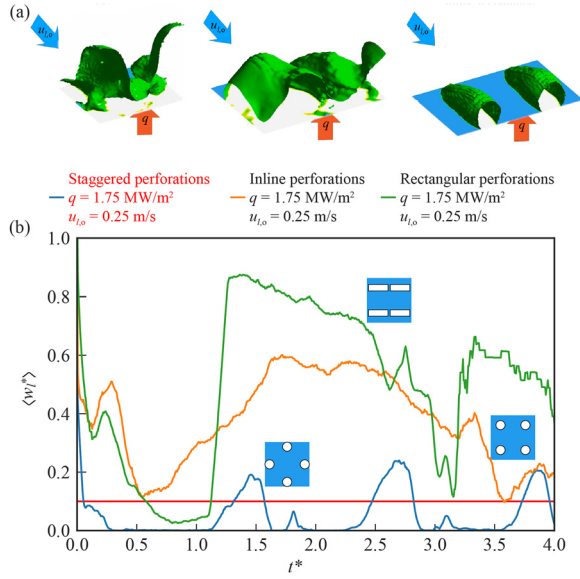


Fig. 8. (a) Schematic representation of vapor sites and surface liquid track snapshots in hexagonal arrangement, aligned with the inlet flow direction, and with rectangular perforations. Red label indicates dryout. The full video is available in the supplementary materials. (b) Time variations of liquid track width at different axial locations for $q = 1.75 \text{ MW/m}^2$, $u_{l,o} = 0.25 \text{ m/s}$ for saturated water (1 atm).

Although the inline circular vapor site arrangement does initially establish a clear path for the liquid flow, this path is taken over by the lateral expansion of vapor, thus nullifying any possible CHF enhancements. The rectangular slot geometry, proposed originally in [26,27,48], with the high aspect ratio $L_{per} : W_{per}$ helps direct the vapor towards the outlet.

Neighboring vapor slots do not coalesce immediately close to the surface ($z = 0$) due to a lateral vapor expansion prevention, imposed by the slot geometry, and axial liquid diversion, thus addressing the shortcomings of the square-aligned circular vapor slots, allowing the formation of a continuous liquid track in the region between perforations.

5.1. Vapor shearing of liquid track

Since the surface liquid track is preserved, no dryout is observed. Further downstream, the surface liquid track continues underneath the flowing vapor. This flow configuration can be approximated by the case of two uniform fluids in relative horizontal motion separated by a horizontal boundary [28], as illustrates Fig. 9(a).

Figure 9 (b) shows snapshots of phase distribution in the flow direction at different axial locations. The evolution of liquid track

is highlighted at two elapsed times, 75 and 150 ms. After enough time, the liquid track in the latter portion of the channel starts to dry and no wetting is observed from the middle of the channel onwards. This marks the geometry modulation limitation.

Since the less dense fluid is on top, this condition is stable, but a critical relative velocity can be found for this flow configuration

$$|\langle u_g \rangle_a - \langle u_l \rangle_a| = \left\{ \frac{2}{\rho_g^* \rho_l^*} \left[\frac{\sigma g (\rho_l^* - \rho_g^*)}{\rho_l^* + \rho_g^*} \right]^{1/2} \right\}^{1/2}, \quad (39)$$

where $\rho_f^* = \rho_f / (\rho_l + \rho_g)$. From Eq. (39), we can infer the acceleration of vapor will eventually trigger the K-H instability. The axial vapor wavelength corresponding to the critical relative velocity is found as

$$\lambda_x = \frac{\pi (u_g - u_l)^2}{g} \frac{\rho_l^* \rho_g^*}{(\rho_l^* - \rho_g^*)}. \quad (40)$$

For liquid-vapor saturated water (1 atm) interfaces, $\lambda_x = 15.7 \text{ mm}$. The relative velocity depends on the heat flux, so a functional relationship of type $q_{CHF,h} \approx \lambda_x^{1/2}$ is found as

$$q_{CHF,KH} = \left[\frac{\lambda_x (\rho_l^* - \rho_g^*)}{\pi \rho_g^* \rho_l^*} g \right]^{1/2} + u_l \left[\frac{\rho_g \Delta h_{lg}}{A_{evap}} \lambda_c^2 \right]. \quad (41)$$

For the given $\lambda_x = 15.7 \text{ mm}$, the maximum heat flux for marginal stability is $q = 5 \text{ MW/m}^2$. The relationship from Eq. (41) is graphically shown in Fig. 9(c) for constant $\lambda_c = 4.5 \text{ mm}$.

5.2. Geometric-confined liquid track

At high heat fluxes, the rectangular slot shape and the liquid inertia might not be enough to prevent the vapor lateral expansion from destabilizing the liquid track. One natural idea is to further enhance the geometric confinement effects described in Section 5.1 by further delaying the merging of neighboring vapor slots.

The addition of levees is schematically shown in Fig. 10(a). Two snapshots at locations from the surface, $z = 0.25$ and 2 mm , show the vapor penetration is considerably reduced in the intralevee spacings (aqueducts), it was first proposed in [26]. The liquid track is shielded from the expanding vapor since a significantly smaller fraction of the vapor diverts towards the liquid track to disturb it. A secondary effect of the addition of levees is the liquid anchoring, due to the no-slip effect, the levees anchor the liquid, further stabilizing it and requiring additional shear from the vapor flow to disrupt it. CFD results show the addition of levees is capable of suppressing the onset of K-H instabilities since the vapor has to penetrate further into the intralevee subchannel, pushing the hydrodynamic CHF to 15 MW/m^2 [26].

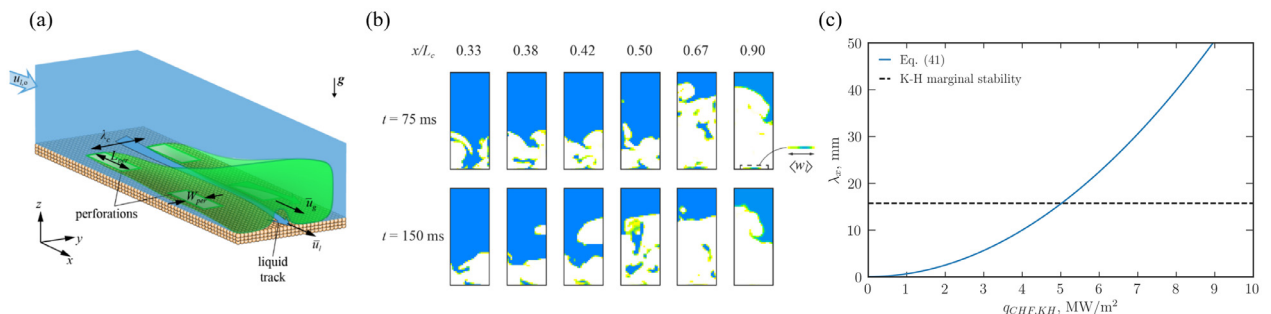


Fig. 9. (a) Rectangular vapor slots aligned with the flow direction. (b) Snapshots of the axial distribution of the liquid track at two distinct elapsed times ($q = 5 \text{ MW/m}^2$, $u_{l,o} = 0.5 \text{ m/s}$). (c) Variations of interfacial vapor wavelength with Kelvin-Helmholtz CHF for $\lambda_c = 4.5 \text{ mm}$. The axial K-H marginal stability is highlighted.

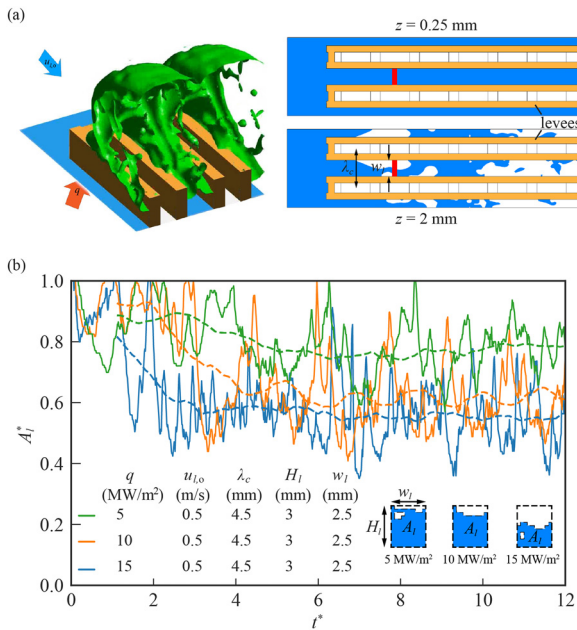


Fig. 10. (a) Snapshot of C-GMR video and top-view of phase distribution in the axial planes at elevations $z = 0.25$ and 2 mm for metasurface with levees. The full video is available in the supplementary materials. (b) Time variation of liquid phase yz area fraction at $x = 16$ mm. $q = 5, 10$ and 15 MW/m², $u_{l,0} = 0.5$ m/s for saturated water (1 atm).

Figure 10 (b) shows the time variation of the dimensionless area of liquid in the intraleeve channel (spanning -1.25 mm $\leq y \leq 1.25$ mm by 0 mm $\leq z \leq 3$ mm) at axial location $x = 16$ mm for different heat fluxes ($q = 5, 10$ and 15 MW/m²). The dimensionless area is calculated according to

$$\langle A_l^* \rangle = \frac{1}{\Delta x} \sum_i \frac{1}{w_l H_l} \int_0^{w_l} \int_0^{H_l} f dz dy, \begin{cases} f = 0, & \alpha \geq 0.5 \\ f = 1, & \alpha < 0.5 \end{cases} \quad (42)$$

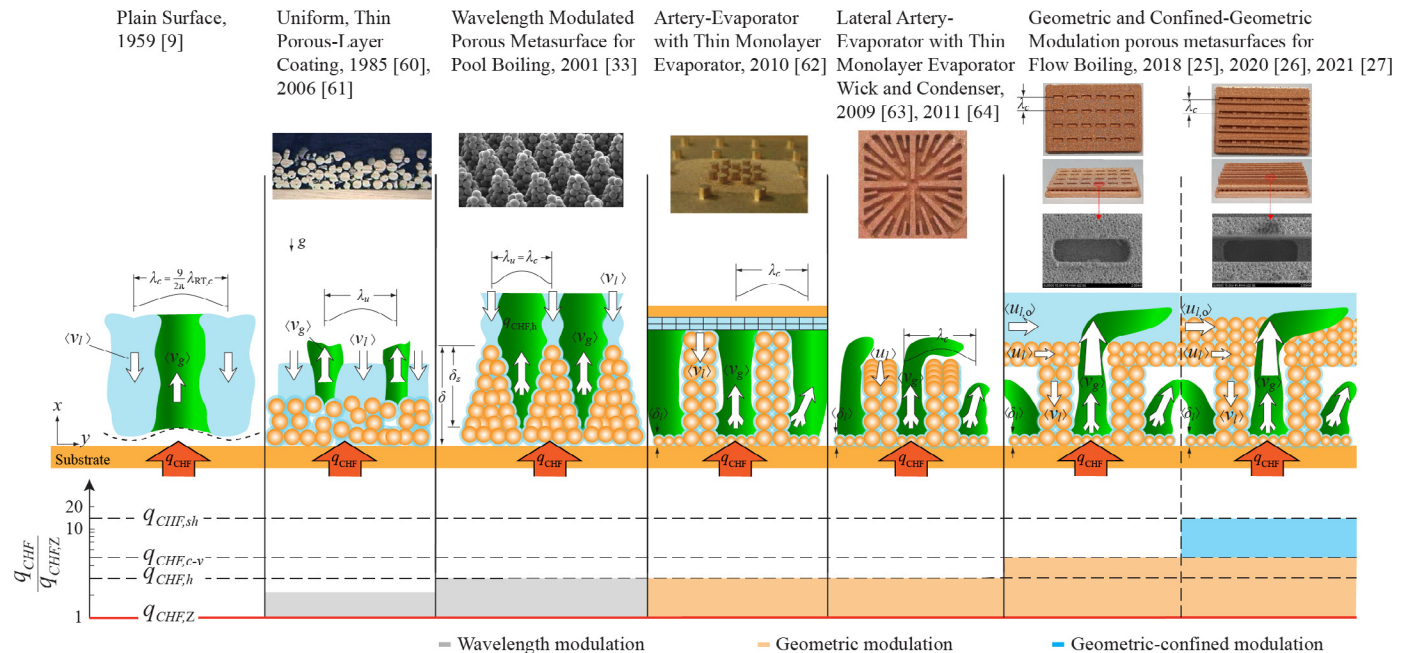


Fig. 11. An evolution of porous metasurfaces for enhanced CHF [59], updated with the flow-boiling canopy wick metasurface [26,48]. The porous coatings are made of sintered copper particles. The corresponding q_{CHF} in the three enhancement regimes, wavelength-modulation, geometric modulation, and confined-geometric modulation, are also shown.

No dryout is observed even though the heat flux was increased to 15 MW/m² at the same inlet velocity of $u_{l,0} = 0.5$ m/s. The higher intensity turbulence is still stemming from the interface, but further away from the liquid track, at the top portion of the channel, where the high-velocity vapor deflects the liquid. As mentioned earlier, inside the intraleeve subchannel, the vapor is at a much lower velocity, so the flow is less turbulent, and the K-H stability is preserved.

6. Porous metasurface for geometric modulation: Capillary-viscous bottleneck

Metasurfaces are unit-cell based, generally 3-D surface structures designed and fabricated for a targeted function. For example, in electromagnetic and sound wave applications they have sub-wavelength features capable of modulating the surface transmission, absorption and refraction from phenomenon of interest [55–57].

As discussed above, in boiling crises, the surface vapor generation triggers interfacial instabilities, and related metasurfaces, including sub-critical wavelength surface modulations have been used [58]. The evolution of boiling metasurfaces for enhancing the CHF is shown in Fig. 11, employing capillary evaporator wicks. It began with a uniform porous coating to reduce the surface superheat [59] and later to also increase the CHF over the plain surface [60]. Figure 11 shows the schematic of metasurfaces and their physical images, as well as the CHF enhancement compared to the Zuber $q_{CHF,Z}$. The shaded areas at the bottom shows the measured enhancement achieved so far in the wavelength modulation, geometric modulation, and geometric-confined modulation regimes.

The first porous metasurface sub-wavelength modulation of the interfacial pool boiling wave was by Liter and Kaviany [33], reducing the superheat and enhancing the CHF using sintered copper particles. The 3-D capillary structures for phase separation using columnar and lateral arteries have been designed for irrigation and evaporative cooling of concentrated heat source [61–64]. In flow boiling, the porous metasurface provides separation for the liquid supply and vapor escape paths, preventing the phase competition

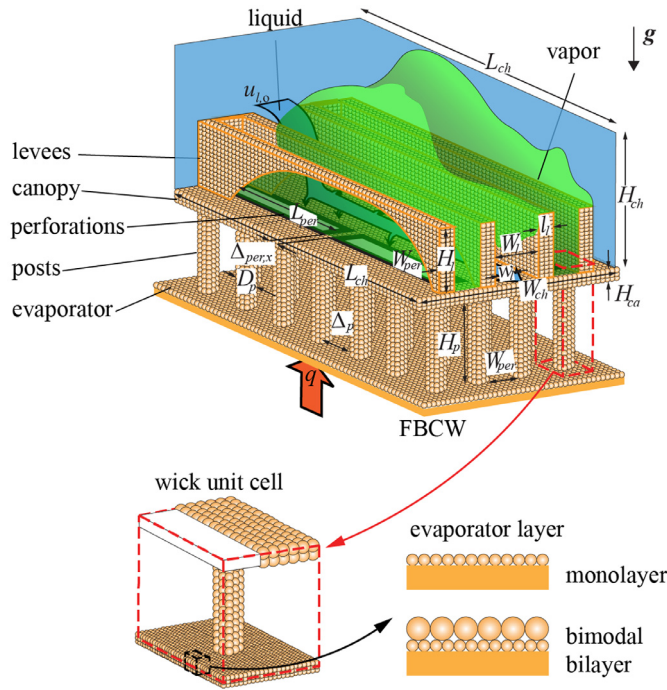


Fig. 12. Schematic illustration of the flow-boiling canopy wick. Adapted from Kim et al. [48].

close to the surface [25]. The wick superheat, capillary-viscous and hydrodynamic q_{CHF} are shown.

Also shown in Fig. 11, is the recent work on raising $q_{CHF,h}$ by preventing the onset of Kelvin-Helmholtz instabilities with the flow-boiling canopy wick (FBCW), a 3-D (and multiscale) porous metasurface that modulates vapor-escape sites (vapor perforations) [25,26], Fig. 12. The FBCW separate of liquid and vapor phases, directs the liquid from the liquid channel to the thin evaporator wick with high capillary pressure capability, and allows for vapor space over the evaporator for achieving large thermal conductance and vapor escape sites (perforations) directing the vapor into the liquid channel. Its three main components are the evaporator, posts, and perforated canopy. All three porous components coordinately direct the liquid towards the heated surface. Liquid is assumed to be saturated in the channel and canopy and post wicks. The thin wick evaporator is responsible for spreading and evaporating the liquid with low resistance (thermal and hydraulic), generating saturated vapor. The posts separate the evaporator and the canopy and form the vapor space. The perforated canopy is where the vapor wavelength modulation occurs, since it separates of the phases and controls of vapor sites entering the liquid channel at regularly spaced perforations. The addition of levees further stabilizes the liquid track formed on the perforated canopy. The high velocity of the liquid being wicked across the canopy and posts leads to high Péclet number, resulting in negligible upstream thermal conduction [33]. At the thin wick evaporator, the sintered particles contribute to an increased effective thermal conductivity, reducing the thermal resistance [27].

The liquid flow path from the channel to the heated surface goes through the canopy, posts, and evaporator layer, and each component has its associated pressure drop. Furthermore, the vapor escape through the perforations causes an additional pressure drop that must also be accounted for by the capillary wick. The combined pressure drops cannot exceed the maximum capillary pressure $p_{c,max}$, i.e.,

$$\sum \Delta p_i = \Delta p_e + \Delta p_p + \Delta p_{ca} + \Delta p_{per,g} \leq p_{c,max}, \quad (43)$$

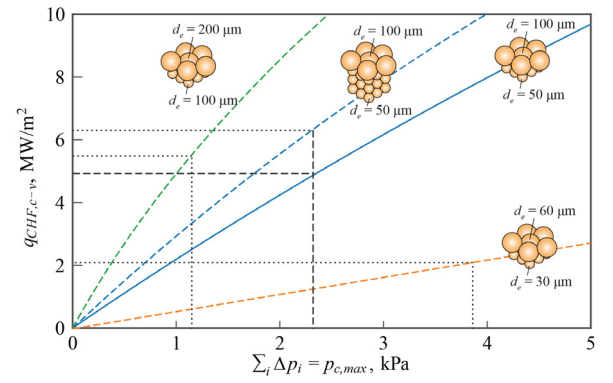


Fig. 13. Variations of the capillary-viscous CHF with the total pressure drop, for four different evaporator wick designs (Table 3) which affect the maximum capillary pressure. Results for saturated water at one atm.

The maximum total pressure drop allowed corresponds to the capillary-viscous heat flux limit (CHF controlled by the evaporator maximum capillary pressure). Equation (43) can be rewritten to relate the heat flux and the maximum capillary pressure, i.e.,

$$\frac{\mu_l L_p'^2}{\rho_l \Delta h_{lg}} \left[\frac{(L_p' - D_p)/3}{K_e} \frac{4}{\langle \delta_l \rangle (L_p' + D_p)/2} + \frac{H_p}{K_p D_p^2} \right] q_{CHF,c-v} + \frac{(A^*)^2 C}{2 \rho_g^2 \Delta h_{lg}} q_{CHF,c-v}^2 = p_{c,max}, \quad (44)$$

where $A^* = \frac{(W_{per} + D_p)(\lambda_c + D_p)}{(W_{per} + D_p)(\lambda_c + D_p - 6\pi D_p^2/4)}$ and $L_p' = \left[\frac{4}{\pi} (W_{per} + D_p)(\Delta_p + D_p) \right]^{1/2}$. The derivation of this quadratic equation is discussed in detail in [27].

Figure 13 shows the variations of the capillary-viscous CHF with the overall pressure drop for different wick designs. Results for the blue curve have been experimentally verified in [48] for a bimodal bilayer wick with particles sized $d_e = 50$ and $100 \mu\text{m}$ with a $p_{c,max} = 2.32 \text{ kPa}$ and the current capillary-viscous CHF is $q_{CHF,c-v} = 4.6 \text{ MW/m}^2$. The orange and green lines are design variations corresponding to $d_e = 30$ and $60 \mu\text{m}$ and $d_e = 100$ and $200 \mu\text{m}$. The smaller particles wick ($p_{c,max} = 3.86 \text{ kPa}$) results in a CHF reduction to $q_{CHF,c-v} = 2.1 \text{ MW/m}^2$ while the large particles wick provide an enhancement despite the $p_{c,max}$ reduction, $q_{CHF,c-v} = 5.5 \text{ MW/m}^2$ ($p_{c,max} = 1.15 \text{ kPa}$). A large enhancement is obtained using a thicker evaporator layer (3 layers): $q_{CHF,c-v} = 6.3 \text{ MW/m}^2$. So, search for raising $q_{CHF,c-v}$, which is the bottleneck to higher $q_{CHF,h}$, continues. The corresponding pressure drops are listed in Table 3. Further details are available in [48].

Figure 14 (a) and (b) show the variations of the hydrodynamic CHF with the critical wavelength λ_c and $u_{l,0}$. The three regimes, namely wavelength, geometry, and geometry-confined modulation with levees, are marked, as well as their transitions (boundaries).

The wavelength-modulation CHF is given by Eqs. (38) and (39) and is primarily controlled by $u_{l,0}$ and presented by the dashed gray line. The inlet velocity reduces the critical wavelength causing higher vapor velocity and increasing the heat flux required to trigger the instability. This enhancement is limited by the smallest physically-limited wavelength, i.e., the capillary length, marked in Fig. 14(a). The 1/6 power-law dependency of the CHF on the inlet velocity is shown in Fig. 14(b) and is in general agreement with the low and high-velocity experimental data.

The geometry modulation, decoupling the wavelength from the inlet velocity, allows for a larger enhancement, as shown by the strip regime in Fig. 14(a). The CFD predictions [26] and experimental results [48–51] are also shown. This enhancement is controlled by the vapor confinement provided by the rectangular per-

Table 3
Pressure drop components for the different evaporator layer designs. The corresponding $q_{CHF,c-v}$ are also listed.

$d_e, \mu\text{m}$	$q_{CHF,c-v}, \text{MW/m}^2$	$G/A, \text{MW/m}^2\text{-K}$	$\Delta p_e, \text{kPa}$	$\Delta p_p, \text{kPa}$	$\Delta p_{ca}, \text{kPa}$	$\Delta p_{per,g}, \text{kPa}$	$\sum \Delta p_i, \text{kPa}$	$p_{c,max}, \text{kPa}$
50,100	5.0	0.25	1.93	0.15	0.04	0.20	2.32	2.32
3060	2.1	0.42	3.67	0.08	0.03	0.08	3.86	3.86
100,200	5.5	0.15	0.58	0.22	0.05	0.28	1.14	1.14
50(3),100	6.3	0.08	1.63	0.29	0.06	0.34	2.32	2.32

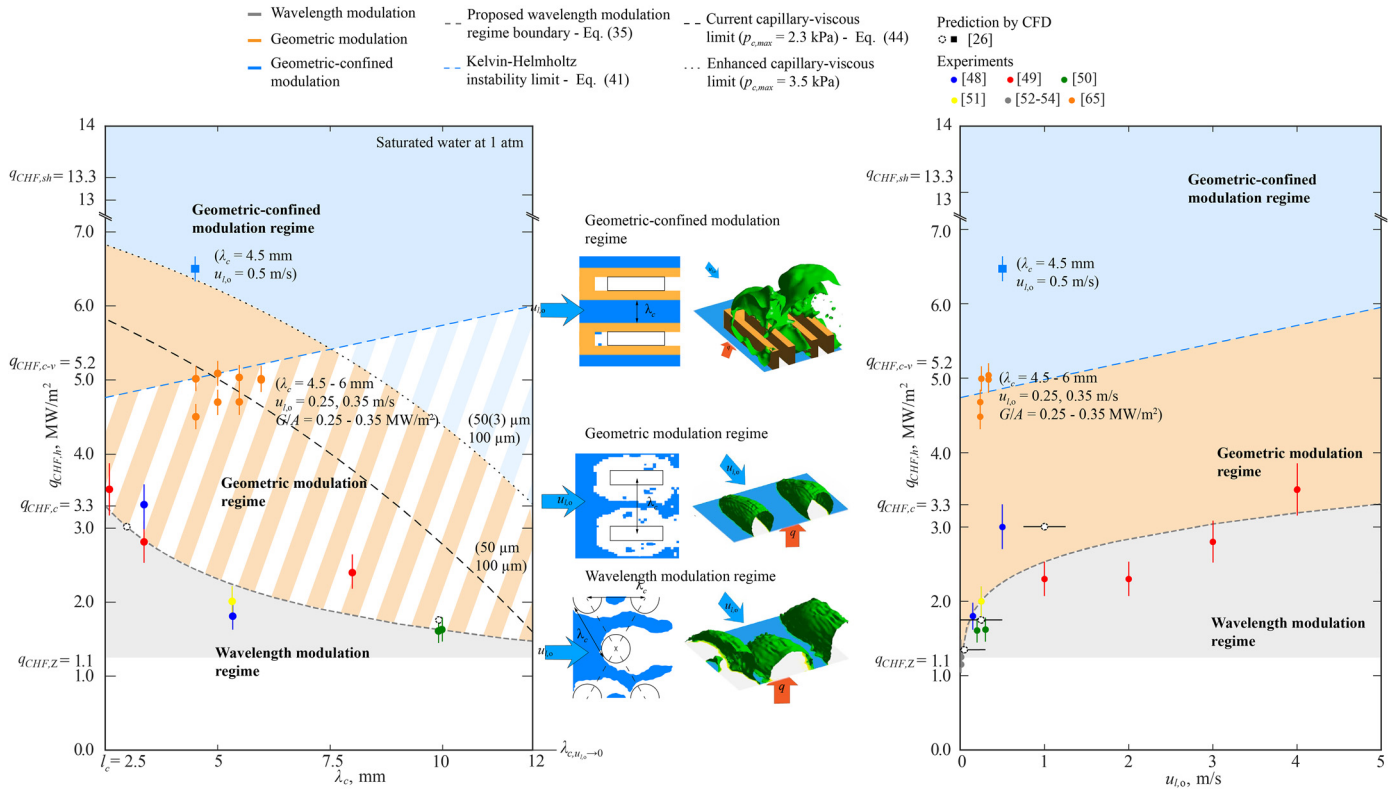


Fig. 14. Regime diagram showing the variations of flow-boiling CHF with (a) wavelength and (b) inlet velocity. The three modulation regimes are highlighted: wavelength modulation, geometric modulation, and geometric-confined modulation, as well as their boundaries. Experimental data and CFD data are also shown. Orange circles denote experimental data for geometric modulation including length scale, inlet velocity and global thermal conductance.

forations, restricting the vapor lateral expansion and preserving the liquid tracks. The orange region in Fig. 14(b) is bound by the $q_{CHF} - u_{l,0}$ relation Eq. (34) at the bottom and the K-H instability Eq. (38) on the top. The capillary-viscous metasurface-imposed limit is not shown since it depends on the characteristic wavelength of the metasurface, which is decoupled from the inlet velocity.

The current results show the limits for the K-H dominated geometry modulation $q_{CHF,h}$ and the porous metasurface $q_{CHF,c-v}$ are rather close, as confirmed by experiments [65], so no further enhancements can be obtained before further improvement to the porous metasurface, i.e., increasing $q_{CHF,c-v}$. After that, to continue increasing the $q_{CHF,h}$, the use of levees is required, i.e., the geometric-confined modulation regime, represented by the blue color in Fig. 14(a), creating the intralevee spacing which effectively raised $q_{CHF,h} > 10 \text{ MW/m}^2$. The wick superheat limit $q_{CHF,sh}$ which marks vapor forming within the evaporation wick is reached there, estimated as 13.3 MW/m^2 for the current FBCW [48]. The measured FBCW thermal conductance G/A which is rather very high is shown in Fig. 14 and listed in Table 3.

7. Conclusions

Direct numerical simulation (DNS), including turbulence, of saturated water (one atm) flow boiling, based on the Zuber pool-

boiling, hydrodynamic instability unit-cell theoretical construct, allows for circular vapor-column site wavelength modulation by the liquid-flow velocity $u_{l,0}$. In the DNS of flow boiling, the vapor and liquid velocities on the heated surface are prescribed, according to the $u_{l,0} = 0$, i.e., the Zuber unit-cell construct. The results for $u_{l,0} > 0$ show a leading-edge, surface liquid track formed on the heated surface. This track meanders between the vapor columns and once the CHF is reached, it becomes unstable and dryout occurs within the first (leading edge) unit cell.

The DNS results show with $u_{l,0}$ as small as 5 cm/s, the inertia is large enough to deflect the Zuber vertical vapor columns and noticeably increase the critical heat flux (CHF) over the Zuber limit $q_{CHF,Z}$. This is called the wavelength-modulation CHF enhancement regime and ranges from this very-low $u_{l,0}$ limit $q_{CHF,Z} = 1.1 \text{ MW/m}^2$ to the capillarity limit of about $q_{CHF,c} = 3.3 \text{ MW/m}^2$, where the wavelength reaches the capillarity length based on the critical Bond number. The predicted range is in good agreement with experiments and a correlation is proposed based on the product of Bond and liquid Reynolds number relating the wavelength and $u_{l,0}$. In this new relation $q_{CHF,h}$ is proportional to $u_{l,0}^{1/6}$.

The DNS results also show that to reach beyond the wavelength-modulation CHF enhancement regime, the vapor site geometry should be anisotropic, with rectangular vapor sites aligned with the flow direction to allow stable leading-edge liquid track. This is called the geometric-modulation regime and upon

optimization of the site geometry can reach the next limit hydrodynamic limit $q_{CHF,h}$ and is over 10 MW/m². This is reached due to vapor shearing (Kelvin-Helmholtz instability) of the liquid track between the vapor sites. To prevent this the liquid tracks are geometrically confined by levees placed around the vapor sites. This geometric-confined CHF enhancement limit is rather very large.

The geometric modulation, including liquid track confinement, are achieved by porous metasurfaces, which are 3-D porous and perforated wicks. One example is the flow-boiling canopy wick (FBCW) which delivers liquid from the above-mentioned liquid tracks formed on a perforated, porous canopy to porous posts and to a thin evaporator wick. The vapor formed over the evaporator flows between posts and escapes through the perforated canopy and mixes with the flowing liquid. While porous metasurfaces allow for realization of the prescribed the surface liquid and vapor velocities in the DNS, they introduce the internal hydrodynamic limit within the porous structure. This is the capillary-viscous limit $q_{CHF,c-v}$ is controlled by the maximum capillary pressure and currently limits the saturated (one atm) water to about 5.2 MW/m².

The summary of the predicted three CHF-enhancement regimes, i.e., the wavelength, geometric, and geometric-confined modulations, and their boundaries, along with the existing experimental results, are shown in Fig. 14.

Author Statement

Julio Ferreira: modeling, formal analysis, visualization, writing - original draft; **Massoud Kaviany:** conceptualization, theory, supervision, writing - review & editing administration.

Declaration of Competing Interest

The authors declare that they have no known competing financial interests or personal relationships that could have appeared to influence the work reported in this paper.

Acknowledgements

This work is supported by NSF USA (Thermal Transport and Processes, CBET16235720). JF is thankful, acknowledging his scholarship supported by CAPES-Brazilian Federal Agency for Support and Evaluation of Graduate Education, within the Ministry of Education (88881.170629/2018-01).

Appendix A. Boiling hydrodynamic instability theory

The results in Section 2 are based on the one treatments in [29] and [30]. An initially stratified two-phase flow may experience interfacial instabilities under relative phasic motion [28], depending on the flow condition, this impacts the heat and mass transfer [29]. The linear stability theory considers the liquid-vapor interface as planar and horizontal with the phases moving with axial velocities u_g and u_l . The disturbance grows axially and with time, and incompressible, inviscid, 2-D base flow is considered. The Navier-Stokes equations are [29]

$$\frac{\partial u_f}{\partial x} + \frac{\partial v_f}{\partial z} = 0, \tag{A.1}$$

$$\rho \left(\frac{\partial u_f}{\partial t} + u_f \frac{\partial u_f}{\partial x} + v_f \frac{\partial u_f}{\partial z} \right) = -\frac{\partial p}{\partial x}, \tag{A.2}$$

$$\rho \left(\frac{\partial v_f}{\partial t} + u_f \frac{\partial v_f}{\partial x} + v_f \frac{\partial v_f}{\partial z} \right) = -\frac{\partial p}{\partial z} - \rho g. \tag{A.3}$$

The velocities and pressure are decomposed into base flow and perturbed components $u_f = \bar{u}_f + u'_f$, $v_f = \bar{v}_f + v'_f$, $p = \bar{p} + p'$. Substituting the decomposed flow quantities into Eqs. (A.1)–(A.3) and performing the required simplifications, we get to

$$\frac{\partial u'_f}{\partial x} + \frac{\partial v'_f}{\partial z} = 0, \tag{A.4}$$

$$\rho \left(\frac{\partial u'_f}{\partial t} + \bar{u}_f \frac{\partial u'_f}{\partial x} \right) = -\frac{\partial p'}{\partial x}, \tag{A.5}$$

$$\rho \left(\frac{\partial v'_f}{\partial t} + \bar{u}_f \frac{\partial v'_f}{\partial x} \right) = -\frac{\partial p'}{\partial z}. \tag{A.6}$$

Differentiating Eqs. (A.5) and (A.6) with respect to x and z , respectively, and adding them together yields the Laplace equation

$$\frac{\partial^2 p'}{\partial x^2} + \frac{\partial^2 p'}{\partial z^2} = 0, \tag{A.7}$$

and the base pressure field for each phase is simply hydrostatic

$$\bar{p}_i = p_o - \rho_i g z. \tag{A.8}$$

The initial interfacial perturbation is considered as a Fourier component of the interfacial wavelength

$$\delta(x, t = 0) = \delta_o e^{i\kappa x}, \tag{A.9}$$

where δ is the perturbation and $\kappa = 2\pi/\lambda$ the wave number. Similarly,

$$\begin{aligned} \delta &= \delta_o e^{i\kappa x + \omega t}, \\ v'_f &= \hat{v}_f(z) e^{i\kappa x + \omega t}, \\ p' &= \hat{p}(z) e^{i\kappa x + \omega t}, \end{aligned} \tag{A.10}$$

where $\omega = 2\pi/f$ is the angular frequency. Using this pressure in Eq. (A.7), we have

$$\frac{d^2 \hat{p}}{dz^2} = \kappa^2 \hat{p}. \tag{A.11}$$

The solution is

$$\hat{p}_i = p_{i,o} e^{\kappa z}, \tag{A.12}$$

Substituting these in Eq. (A.6), we obtain

$$\hat{v}_f(z) = -[\rho(\omega + i\kappa \bar{u}_f)]^{-1} \left(\frac{d\hat{p}}{dz} \right). \tag{A.13}$$

Evaluating the pressure gradient from Eq. (A.12), the velocities are found and when using the functional form for the decomposed perturbed flow results in a differential equation for the perturbed axial velocity. This expression is integrated using the condition $u'_f \rightarrow 0$ far from the interface and gives

$$u'_f = \frac{i}{\kappa} \left(\frac{d\hat{v}_f}{dz} \right) e^{i\kappa x + \omega t}. \tag{A.14}$$

With this solution for the perturbed flow, the boundary conditions are applied at the interface starting with

$$v'_f = \frac{\partial \delta}{\partial t} + \bar{u}_f \frac{\partial \delta}{\partial x}, \tag{A.15}$$

and imposing this condition and substituting Eqs. (A.10) and (A.13) into Eq. (A.15) gives

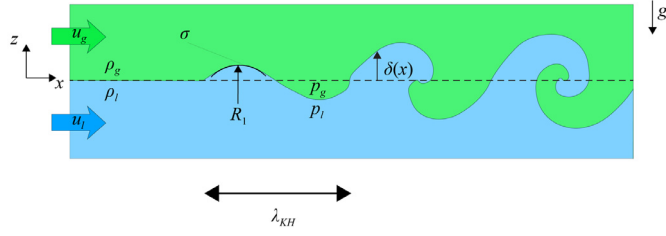


Fig. A1. Evolution of interfacial instability on a horizontal liquid-vapor interface and the Kelvin-Helmholtz instability and wavelength.

$$\begin{aligned} \kappa p_{g,o} [\rho_g (\omega + ik \bar{u}_g)]^{-1} &= \delta_o \omega + i \delta_o \kappa \bar{u}_g, \\ -\kappa p_{l,o} [\rho_l (\omega + ik \bar{u}_l)]^{-1} &= \delta_o \omega + i \delta_o \kappa \bar{u}_l. \end{aligned} \quad (\text{A.16})$$

Solving these equations for $p_{f,o}$ gives

$$\begin{aligned} p_{g,o} &= \frac{\rho_g}{\kappa} (\omega + ik \bar{u}_g)^2 \delta_o, \\ p_{l,o} &= -\frac{\rho_l}{\kappa} (\omega + ik \bar{u}_l)^2 \delta_o. \end{aligned} \quad (\text{A.17})$$

The momentum balance normal to the interface gives [30]

$$p_l - p_g = \sigma \left(\frac{1}{R_1} + \frac{1}{R_2} \right) + 2\mu_l \left(\frac{\partial v_l}{\partial z} - \frac{\partial v_g}{\partial z} \right). \quad (\text{A.18})$$

In the absence of phase change, the second term on the RHS is null and it reduces to the Young-Laplace equation, where $1/R_1$ is the interfacial Euler curvature

$$\frac{1}{R_1} = \frac{\frac{d^2 \delta}{dx^2}}{\left[1 + \left(\frac{d\delta}{dx} \right)^2 \right]^{3/2}}, \quad (\text{A.19})$$

and here (2-D), the other principal curvature is $1/R_2 = 0$. Substituting the curvature into Eq. (A.18), recalling that $p_f = \bar{p}_f + p'_f$, we obtain

$$p_{l,o} - p_{g,o} = \delta_o [(\rho_l - \rho_g)g + \sigma \kappa^2]. \quad (\text{A.20})$$

Substituting Eq. (A.17) into Eq. (A.20) the angular frequency is

$$\begin{aligned} \omega = \pm \frac{\left\{ \kappa^2 \rho_l \rho_g (\bar{u}_l - \bar{u}_g)^2 - [\sigma \kappa^3 + (\rho_l - \rho_g)g\kappa] (\rho_l + \rho_g) \right\}^{1/2}}{\rho_l + \rho_g} \\ - \frac{ik(\rho_l \bar{u}_l + \rho_g \bar{u}_g)}{\rho_l + \rho_g}. \end{aligned} \quad (\text{A.21})$$

Both the surface tension and gravitational acceleration are stabilizing forces. The instability will occur when Eq. (A.21) has a real positive solution, i.e.,

$$\|\bar{u}_l - \bar{u}_g\| > \left\{ \frac{\left[\frac{2\pi\sigma}{\lambda} + \frac{(\rho_l - \rho_g)g\lambda}{2\pi} \right] (\rho_l + \rho_g)}{\rho_l \rho_g} \right\}^{1/2}. \quad (\text{A.22})$$

A critical wavelength can be derived from Eq. (A.22) by setting it to zero. This type of instability is referred to as Kelvin-Helmholtz instability, shown in Fig. A.1. Its wavelength is given in Eq. (1).

When the velocities $u_l = u_g = 0$, with the change in sign of gravity representing the dense fluid on top, we have the Rayleigh-Taylor instability, as illustrates Fig. A.2. The critical wavelength for the Rayleigh-Taylor instability is identical to Eq. (2), but the angular frequency is found by using these velocities and gravity term, and Eq. (A.22) becomes

$$\omega = \pm \left[\frac{(\rho_l - \rho_g)g2\pi/\lambda - \sigma(2\pi/\lambda)^3}{\rho_l + \rho_g} \right]^{1/2}, \quad (\text{A.23})$$

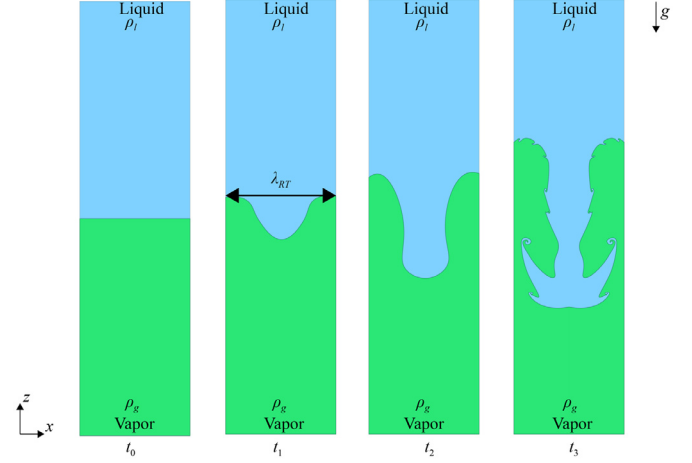


Fig. A2. Evolution of the interfacial instability on horizontal liquid-vapor interface and the formation of the Rayleigh-Taylor instability and wavelength.

with $\rho_l + \rho_g \approx \rho_l$, we have

$$\omega = \pm \left[\frac{(\rho_l - \rho_g)g2\pi/\lambda}{\rho_l} - \frac{\sigma(2\pi/\lambda)^3}{\rho_l} \right]^{1/2}. \quad (\text{A.24})$$

The maximum is found and the wavelength corresponding to this maximum is the most dangerous wavelength $\lambda_{RT,d}$, given by Eq. (2).

The above analysis and results, although simplified, are experimentally verified. A similar decomposition including the thermo-mechanical wave propagation is presented in [30]. In the flow-boiling DNS, we use 3-D fluid flow to track the phase and define surface liquid track dryout.

Appendix B. LES turbulent treatment

In ANSYS Fluent [38], the finite-volume discretization provides the filtering operation for the LES as

$$\tilde{\phi}(\mathbf{x}) = \frac{1}{V} \int_V \phi(\mathbf{x}') d\mathbf{x}', \quad (\text{B.1})$$

where V is the computational cell volume. The filter function is then

$$G(\mathbf{x}, \mathbf{x}') = \begin{cases} \frac{1}{V}, & \mathbf{x}' \in V \\ 0, & \text{otherwise} \end{cases}. \quad (\text{B.2})$$

The filtered Navier-Stokes equations are given in Eqs. (24) and (25). The viscosity stress and the subgrid-scale stress tensors are given as

$$\sigma_{ij} = \left[\mu_f \left(\frac{\partial \tilde{u}_{f,i}}{\partial x_j} + \frac{\partial \tilde{u}_{f,j}}{\partial x_i} \right) \right] - \frac{2}{3} \mu_f \frac{\partial \tilde{u}_{f,l}}{\partial x_l} \delta_{ij}, \quad (\text{B.3})$$

$$\tau_{ij} = \rho_f u_{f,i} \tilde{u}_{f,j} - \rho_f \tilde{u}_{f,i} \tilde{u}_{f,j}. \quad (\text{B.4})$$

To generate a time-independent inlet condition, a random 2-D vortex is considered. With this approach, a perturbation is added on a specified mean velocity profile via a fluctuating vorticity field (i.e., two-dimensional in the plane normal to the streamwise direction). The subgrid-scale resulting from the filtering operation requires modeling. As in RANS, the Boussinesq hypothesis is employed and the stresses are calculated from Eq. (26).

The strain tensor is defined as

$$\bar{S}_{ij} = \frac{1}{2} \left(\frac{\partial \tilde{u}_{f,i}}{\partial x_j} + \frac{\partial \tilde{u}_{f,j}}{\partial x_i} \right). \quad (\text{B.5})$$

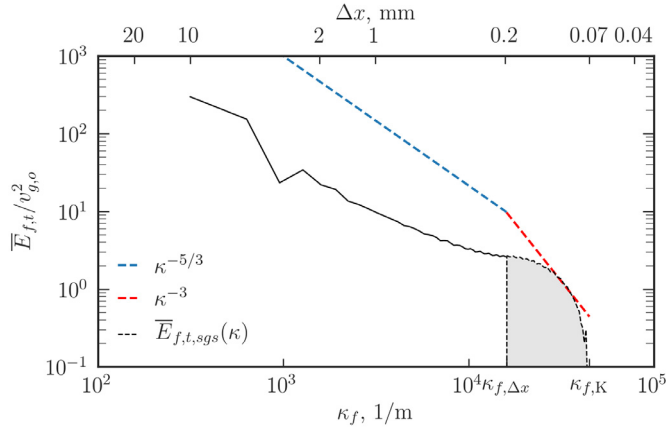


Fig. B1. Turbulence kinetic energy spectra in the axial midplane for (a) plain surface $q = 1.75 \text{ MW/m}^2$ and $u_{t,o} = 0.5 \text{ m/s}$. The Kolmogorov inertial subrange $-5/3$ [42] and the empirical dissipation range -3 [45,67] scales are shown. The subgrid turbulence kinetic energy is highlighted in gray shade.

In the Wall-Adapting Local Eddy-Viscosity (WALE) [66] the eddy viscosity is modeled by

$$\mu_{f,t} = \rho_f L_s^2 \frac{(S_{ij}^d S_{ij}^d)^{3/2}}{(S_{ij} S_{ij})^{5/2} + (S_{ij}^d S_{ij}^d)^{5/4}}, \quad (\text{B.6})$$

where L_s is the mixing length for the subgrid scale

$$L_s = \min(\kappa \Delta z, C_w V^{1/3}), \quad (\text{B.7})$$

where κ is the von Karman constant, $C_w = 0.325$, $V^{1/3}$ is the local grid scale and

$$S_{ij}^d = \frac{1}{2} \left[\left(\frac{\partial \bar{u}_{f,i}}{\partial x_j} \right)^2 + \left(\frac{\partial \bar{u}_{f,j}}{\partial x_i} \right)^2 \right] - \frac{1}{3} \delta_{ij} \left(\frac{\partial \bar{u}_{f,k}}{\partial x_k} \right)^2. \quad (\text{B.8})$$

The interfacial force term in the momentum conservation equation is given by the continuum surface force (CSF) model as

$$\mathbf{f}_s = \sigma \frac{\rho_f \kappa_g \nabla \alpha}{\frac{1}{2}(\rho_l + \rho_g)}, \quad (\text{B.9})$$

where $\kappa_g = \nabla \cdot (\nabla \alpha / \alpha)$ is the interface normal defined as the gradient of the volume fraction.

In order to compute turbulent quantities, a decomposition is required and the velocity resolved by the grid can be decomposed into mean and fluctuation quantities [42]

$$\bar{u}_f = \tilde{u}_f - u'_f, \quad (\text{B.10})$$

where \tilde{u}_f is the filtered velocity field, \bar{u}_f is the mean velocity field averaged over a period of time Δt and u'_f is the fluctuation velocity field. The turbulence kinetic energy resolved by the grid is calculated as

$$\bar{E}_{f,t} = \frac{1}{2} (\bar{u}_f'^2 + \bar{v}_f'^2 + \bar{w}_f'^2). \quad (\text{B.11})$$

The unresolved portion of the turbulent kinetic energy is the subgrid component, in the WALE model [36], this portion of the turbulence kinetic energy is calculated as

$$\bar{E}_{f,t,sgs} = \left(\frac{\mu_{f,t}}{C_w \rho_f L_s} \right)^2. \quad (\text{B.12})$$

The total kinetic energy is, then

$$\bar{E}_{f,t,total} = \bar{E}_{f,t} + \bar{E}_{f,t,sgs}. \quad (\text{B.13})$$

When $\frac{\bar{E}_{f,t}}{\bar{E}_{f,t,total}} \geq 0.8$, the mesh is well suited. For Fig. B.1 and similar results, the ratio is 0.96.

Figure B.1 shows the dimensionless turbulence spectra for $q = 1.75 \text{ MW/m}^2$ on plain surface. The Kolmogorov $-5/3$ power is shown as a blue dashed line in the inertial subrange. The subgrid turbulence kinetic energy decay is highlighted in gray. In the subgrid modeling range, for wavenumbers larger than the filter length,

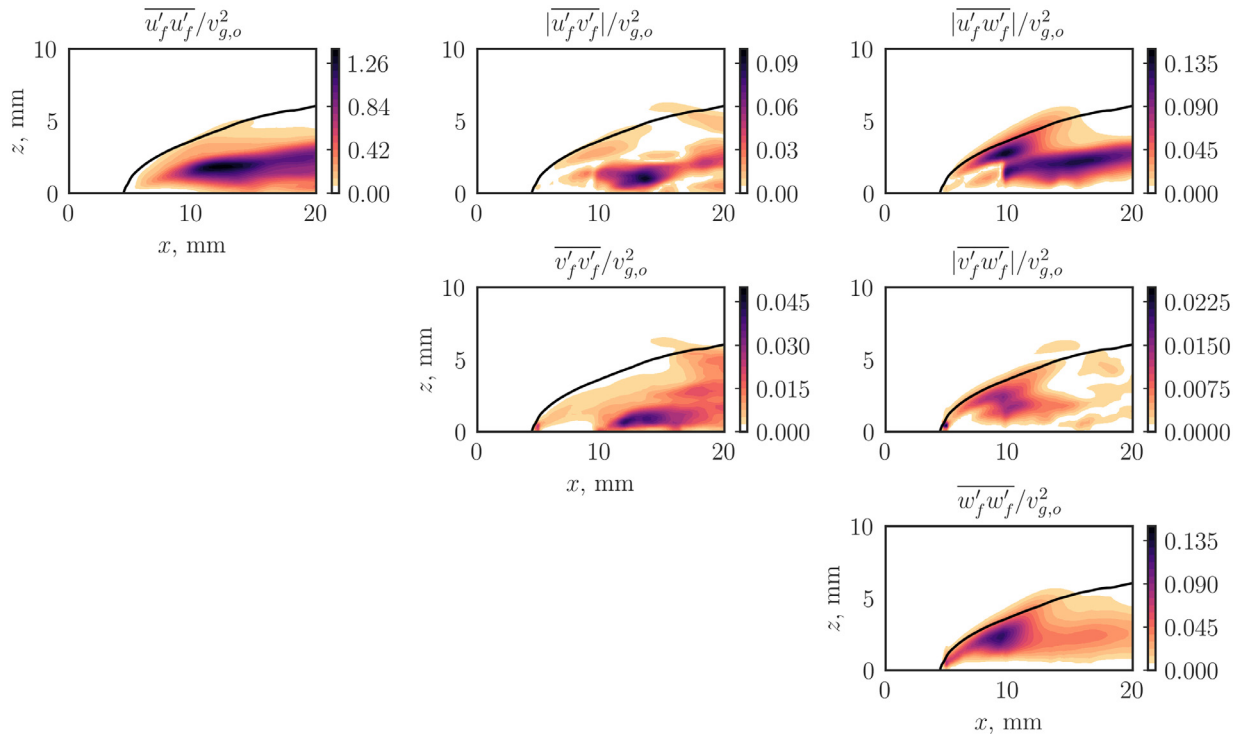


Fig. B2. The distributions of the Reynolds stress tensor components in the axial midplane for $q = 1.75 \text{ MW/m}^2$ and $u_{t,o} = 0.5 \text{ m/s}$ for saturated water (1 atm). The interface is shown with the curved solid line.

i.e., in the dissipation subrange, the spectrum follows the -3 power of the dissipation scale observed experimentally for bubbly flows [45,67]. This is reasonable since the overall observation is that turbulence originates from eddies formed at the liquid-vapor interface and the smallest eddies would be encountered in the small vapor inclusions that detach from the escaping vapor stream. The highest wavenumber which can be resolved by the simulation corresponds to twice the grid size and is denoted as

$$\kappa_{f,\Delta x} = \frac{2\pi}{2L_s}. \quad (\text{B.14})$$

The maximum wavenumber is related to the Kolmogorov length scale, given as [42]

$$\lambda_{f,K} = \left(\frac{\nu_g^3}{\epsilon_{f,t}} \right)^{1/4}. \quad (\text{B.15})$$

These are also marked in Fig. B.1. These and the power-law comparisons in Fig. B.1 support that the numerically predicted turbulent quantities have the expected theoretical behavior.

A similar trend is encountered with the components of the Reynolds stress tensor, as shows Fig. B.2. Results were averaged over a similar time frame. Turbulence intensity is expected to be more pronounced near the channel walls and the liquid-vapor interface. Figure B.2 shows that the most intense stresses occur in the vapor phase, indicating the production of turbulence is more pronounced in the gas phase due to the large inertial force and interfacial shearing.

Supplementary material

Supplementary material associated with this article can be found, in the online version, at [10.1016/j.ijheatmasstransfer.2022.123051](https://doi.org/10.1016/j.ijheatmasstransfer.2022.123051).

References

- [1] D.E. Kim, D.I. Yu, D.W. Jerng, M.H. Kim, H.S. Ahn, Review of boiling heat transfer enhancement on micro/nanostructured surfaces, *Exp. Therm. Fluid Sci.* 66 (2015) 173–196, doi:[10.1016/j.expthermflusci.2015.03.023](https://doi.org/10.1016/j.expthermflusci.2015.03.023).
- [2] M. Dadhich, O.S. Prajapati, V. Sharma, A systematic review on the heat transfer investigation of the flow boiling process, *Chem. Eng. Process. Process Intensif.* 165 (2021) 108425, doi:[10.1016/j.ccep.2021.108425](https://doi.org/10.1016/j.ccep.2021.108425).
- [3] K. Leong, J. Ho, K. Wong, A critical review of pool and flow boiling heat transfer of dielectric fluids on enhanced surfaces, *Appl. Therm. Eng.* 112 (2017) 999–1019, doi:[10.1016/j.applthermaleng.2016.10.138](https://doi.org/10.1016/j.applthermaleng.2016.10.138).
- [4] R. Balasubramaniam, E. Rame, J. Kizito, M. Kassemi, Two Phase Flow Modeling: Summary of Flow Regimes and Pressure Drop Correlations in Reduced and Partial Gravity, Technical Report, National Center for Space Exploration Research, 2006 <https://ntrs.nasa.gov/archive/nasa/casi.ntrs.nasa.gov/20060008906.pdf>.
- [5] C.R. Kharangate, I. Mudawar, Review of computational studies on boiling and condensation, *Int. J. Heat Mass Transf.* 108 (2017) 1164–1196, doi:[10.1016/j.ijheatmasstransfer.2016.12.065](https://doi.org/10.1016/j.ijheatmasstransfer.2016.12.065).
- [6] N.I. Kolev, *Multiphase Flow Dynamics 4*, Springer, 2012 <https://link.springer.com/book/10.1007/978-3-642-20749-5>.
- [7] B. Magolan, E. Baglietto, C. Brown, I.A. Bolotnov, G. Tryggvason, J. Lu, Multiphase turbulence mechanisms identification from consistent analysis of direct numerical simulation data, *Nucl. Eng. Technol.* 49 (6) (2017) 1318–1325, doi:[10.1016/j.net.2017.08.001](https://doi.org/10.1016/j.net.2017.08.001). Special Issue on International Conference on Mathematics and Computational Methods Applied to Nuclear Science and Engineering 2017 (M&C 2017)
- [8] T.Q.D. Pham, J. Jeon, D. Jo, S. Choi, Two-phase flow simulations using 1D centerline-based C- and U-shaped pipe meshes, *Appl. Sci.* 11 (5) (2021), doi:[10.3390/app11052020](https://doi.org/10.3390/app11052020).
- [9] N. Zuber, Hydrodynamic aspects of boiling heat transfer, University of California, Los Angeles, 1959 Ph.D. thesis <https://www.osti.gov/biblio/4175511>.
- [10] J.H. Lienhard, V.K. Dhir, Hydrodynamic prediction of peak pool-boiling heat fluxes from finite bodies, *J. Heat Transf.* 95 (2) (1973) 152–158, doi:[10.1115/1.3450013](https://doi.org/10.1115/1.3450013).
- [11] P.J. Berenson, Film-Boiling heat transfer from a horizontal surface, *J. Heat Transf.* 83 (3) (1961) 351–356, doi:[10.1115/1.3682280](https://doi.org/10.1115/1.3682280).
- [12] L. Zhang, S. Gong, Z. Lu, P. Cheng, E.N. Wang, Boiling crisis due to bubble interactions, *Int. J. Heat Mass Transf.* 182 (2022) 121904, doi:[10.1016/j.ijheatmasstransfer.2021.121904](https://doi.org/10.1016/j.ijheatmasstransfer.2021.121904).
- [13] Q.æ. Li, Y.ä. Yu, Z.X.æ. Wen, How does boiling occur in lattice Boltzmann simulations? *Phys. Fluids* 32 (9) (2020) 093306, doi:[10.1063/5.0015491](https://doi.org/10.1063/5.0015491).
- [14] S. Gong, L. Zhang, P. Cheng, E.N. Wang, Understanding triggering mechanisms for critical heat flux in pool boiling based on direct numerical simulations, *Int. J. Heat Mass Transf.* 163 (2020) 120546, doi:[10.1016/j.ijheatmasstransfer.2020.120546](https://doi.org/10.1016/j.ijheatmasstransfer.2020.120546).
- [15] C. Konishi, I. Mudawar, Review of flow boiling and critical heat flux in microgravity, *Int. J. Heat Mass Transf.* 80 (2015) 469–493, doi:[10.1016/j.ijheatmasstransfer.2014.09.017](https://doi.org/10.1016/j.ijheatmasstransfer.2014.09.017).
- [16] M. Bruder, G. Bloch, T. Sattelmayer, Critical heat flux in flow boiling—review of the current understanding and experimental approaches, *Heat Transf. Eng.* 38 (3) (2017) 347–360, doi:[10.1080/01457632.2016.1189274](https://doi.org/10.1080/01457632.2016.1189274).
- [17] J. Galloway, I. Mudawar, CHF mechanism in flow boiling from a short heated wall—i. examination of near-wall conditions with the aid of photomicrography and high-speed video imaging, *Int. J. Heat Mass Transf.* 36 (10) (1993) 2511–2526, doi:[10.1016/S0017-9310\(05\)80190-5](https://doi.org/10.1016/S0017-9310(05)80190-5).
- [18] J. Sturgis, I. Mudawar, Critical heat flux in a long, rectangular channel subjected to one-sided heating—II. Analysis of critical heat flux data, *Int. J. Heat Mass Transf.* 42 (10) (1999) 1849–1862, doi:[10.1016/S0017-9310\(98\)00275-0](https://doi.org/10.1016/S0017-9310(98)00275-0).
- [19] C.-N. Huang, C.R. Kharangate, A new mechanistic model for predicting flow boiling critical heat flux based on hydrodynamic instabilities, *Int. J. Heat Mass Transf.* 138 (2019) 1295–1309, doi:[10.1016/j.ijheatmasstransfer.2019.04.103](https://doi.org/10.1016/j.ijheatmasstransfer.2019.04.103).
- [20] K. Ling, S. Zhang, W. Liu, X. Sui, W. Tao, Interface tracking simulation for subcooled flow boiling using VOSET method, *Front. Energy Res.* 8 (2021) 325, doi:[10.3389/feng.2020.526035](https://doi.org/10.3389/feng.2020.526035).
- [21] R. Revellin, J.R. Thome, A theoretical model for the prediction of the critical heat flux in heated microchannels, *Int. J. Heat Mass Transf.* 51 (5) (2008) 1216–1225, doi:[10.1016/j.ijheatmasstransfer.2007.03.002](https://doi.org/10.1016/j.ijheatmasstransfer.2007.03.002).
- [22] T.J. Zhang, S. Chen, E.N. Wang, A separated-flow model for predicting flow boiling critical heat flux and pressure drop characteristics in microchannels, in: ASME 2012 10th International Conference on Nanochannels, Microchannels, and Minichannels, in: International Conference on Nanochannels, Microchannels, and Minichannels, 2012, pp. 39–48, doi:[10.1115/ICNMM2012-73046](https://doi.org/10.1115/ICNMM2012-73046).
- [23] J. Broughton, Y.K. Joshi, Flow boiling in geometrically modified microchannels, *Phys. Fluids* 33 (10) (2021) 103308, doi:[10.1063/5.0062585](https://doi.org/10.1063/5.0062585).
- [24] G. Liang, I. Mudawar, Review of channel flow boiling enhancement by surface modification, and instability suppression schemes, *Int. J. Heat Mass Transf.* 146 (2020) 118864, doi:[10.1016/j.ijheatmasstransfer.2019.118864](https://doi.org/10.1016/j.ijheatmasstransfer.2019.118864).
- [25] M. Kim, M. Kaviany, Flow-boiling canopy wick for extreme heat transfer, *Int. J. Heat Mass Transf.* 117 (2018) 1158–1168, doi:[10.1016/j.ijheatmasstransfer.2017.10.079](https://doi.org/10.1016/j.ijheatmasstransfer.2017.10.079).
- [26] J. Ferreira, M. Kaviany, Geometric-confinement suppression of flow-boiling instability using perforated wick: Part I CHF and conductance enhancement, *Int. J. Heat Mass Transf.* 159 (2020) 120080, doi:[10.1016/j.ijheatmasstransfer.2020.120080](https://doi.org/10.1016/j.ijheatmasstransfer.2020.120080).
- [27] J. Ferreira, M. Kaviany, Geometric-confinement suppression of flow-boiling instability using perforated wick: Part II CHF limits and wick properties, *Int. J. Heat Mass Transf.* 159 (2020) 120079, doi:[10.1016/j.ijheatmasstransfer.2020.120079](https://doi.org/10.1016/j.ijheatmasstransfer.2020.120079).
- [28] S. Chandrasekhar, *The stability of superposed fluids: the Kelvin-Helmholtz instability, in: Hydrodynamic and Hydromagnetic Stability, in: International Series of Monographs on Physics*, Clarendon Press, 1961, pp. 481–514.
- [29] V.P. Carey, *Convective Boiling in Tubes and Channels, in: Liquid-Vapor Phase-Change Phenomena*, Taylor & Francis, 1992, pp. 483–562.
- [30] M. Kaviany, *Carrier Energy Transport and Transformation Theories*, in: *Heat Transfer Physics*, 2nd ed., Cambridge University Press, 2014, pp. 119–172. <https://doi.org/10.1017/CBO9781107300828>.
- [31] H. Kim, J.C. Padrino, D.D. Joseph, Viscous effects on Kelvin-Helmholtz instability in a channel, *J. Fluid Mech.* 680 (2011) 398–416, doi:[10.1017/jfm.2011.206](https://doi.org/10.1017/jfm.2011.206).
- [32] V. Sernas, J. Lienhard, V. Dhir, The Taylor wave configuration during boiling from a flat plate, *Int. J. Heat Mass Transf.* 16 (9) (1973) 1820–1821, doi:[10.1016/0017-9310\(73\)90175-0](https://doi.org/10.1016/0017-9310(73)90175-0).
- [33] S.G. Lister, M. Kaviany, Pool-boiling CHF enhancement by modulated porous-layer coating: theory and experiment, *Int. J. Heat Mass Transf.* 44 (22) (2001) 4287–4311, doi:[10.1016/S0017-9310\(01\)00084-9](https://doi.org/10.1016/S0017-9310(01)00084-9).
- [34] A. Bar-Cohen, A. McNeil, Parametric effects on pool boiling critical heat flux in dielectric liquids, in: *Pool and External Flow Boiling*, 1992, pp. 171–175.
- [35] S.S. Kutateladze, A.I. Leont'ev, Some applications of the asymptotic theory of the turbulent boundary layer, in: *International Heat Transfer Conference*, vol. 3, 1966, pp. 1–6.
- [36] J. Weisman, B. Pei, Prediction of critical heat flux in flow boiling at low qualities, *Int. J. Heat Mass Transf.* 26 (10) (1983) 1463–1477, doi:[10.1016/S0017-9310\(83\)80047-7](https://doi.org/10.1016/S0017-9310(83)80047-7).
- [37] C. Lee, I. Mudawar, A mechanistic critical heat flux model for subcooled flow boiling based on local bulk flow conditions, *Int. J. Multiphase Flow* 14 (6) (1988) 711–728, doi:[10.1016/0301-9322\(88\)90070-5](https://doi.org/10.1016/0301-9322(88)90070-5).
- [38] *Fluent Reference Manual*, ANSYS, 2009.
- [39] G. Tomar, G. Biswas, A. Sharma, A. Agrawal, Numerical simulation of bubble growth in film boiling using a coupled level-set and volume-of-fluid method, *Phys. Fluids* 17 (11) (2005) 112103, doi:[10.1063/1.2136357](https://doi.org/10.1063/1.2136357).
- [40] R. Courant, F. K. H. Lewy, On the partial difference equations of mathematical physics, *Math. Ann.* 100 (1) (1928) 32–74, doi:[10.1006/1.2136357](https://doi.org/10.1006/1.2136357).
- [41] P. Sagaut, Application to Navier–Stokes Equations, in: *Large Eddy Simulation for Incompressible Flows: An Introduction*, Springer Berlin Heidelberg, Berlin, Heidelberg, 2006, pp. 45–81. https://doi.org/10.1007/3-540-26403-5_3.
- [42] S.B. Pope, *Turbulent Flows*, Cambridge University Press, 2000, doi:[10.1017/CBO9780511840531](https://doi.org/10.1017/CBO9780511840531).

- [43] J. Jeong, F. Hussain, On the identification of a vortex, *J. Fluid Mech.* 285 (1995) 69–94, doi:[10.1017/S0022112095000462](https://doi.org/10.1017/S0022112095000462).
- [44] J.-m. Zhan, Y.-t. Li, W.-h.O. Wai, W.-q. Hu, Comparison between the Q criterion and Rortex in the application of an in-stream structure, *Phys. Fluids* 31 (12) (2019) 121701, doi:[10.1063/1.5124245](https://doi.org/10.1063/1.5124245).
- [45] S. Long, J. Yang, X. Huang, G. Li, W. Shi, M. Sommerfeld, X. Yang, Large-eddy simulation of gas-liquid two-phase flow in a bubble column reactor using a modified sub-grid scale model with the consideration of bubble-eddy interaction, *Int. J. Heat Mass Transf.* 161 (2020) 120240, doi:[10.1016/j.ijheatmasstransfer.2020.120240](https://doi.org/10.1016/j.ijheatmasstransfer.2020.120240).
- [46] M. Saeedipour, S. Puttinger, N. Doppelhammer, S. Pirker, Investigation on turbulence in the vicinity of liquid-liquid interfaces - large eddy simulation and PIV experiment, *Chem. Eng. Sci.* 198 (2019) 98–107, doi:[10.1016/j.ces.2018.12.040](https://doi.org/10.1016/j.ces.2018.12.040).
- [47] M. Saeedipour, S. Schneiderbauer, Favre-filtered LES-VOF of two-phase flows with eddy viscosity-based subgrid closure models: an a-posteriori analysis, *Int. J. Multiphase Flow* 144 (2021) 103780, doi:[10.1016/j.ijmultiphaseflow.2021.103780](https://doi.org/10.1016/j.ijmultiphaseflow.2021.103780).
- [48] T.K. Kim, J. Ferreira, H. Jo, M. Kaviany, Flow-boiling canopy wick capillary-viscous limit, *Int. J. Heat Mass Transf.* 181 (2021) 121999, doi:[10.1016/j.ijheatmasstransfer.2021.121999](https://doi.org/10.1016/j.ijheatmasstransfer.2021.121999).
- [49] H.S. Ahn, H. Kim, H. Jo, S. Kang, W. Chang, M.H. Kim, Experimental study of critical heat flux enhancement during forced convective flow boiling of nanofluid on a short heated surface, *Int. J. Multiphase Flow* 36 (5) (2010) 375–384, doi:[10.1016/j.ijmultiphaseflow.2010.01.004](https://doi.org/10.1016/j.ijmultiphaseflow.2010.01.004).
- [50] T. Lee, D.H. Kam, J.H. Lee, Y.H. Jeong, Effects of two-phase flow conditions on flow boiling CHF enhancement of magnetite-water nanofluids, *Int. J. Heat Mass Transf.* 74 (2014) 278–284, doi:[10.1016/j.ijheatmasstransfer.2014.03.028](https://doi.org/10.1016/j.ijheatmasstransfer.2014.03.028).
- [51] P. Weber, K. Johansson, Study of the critical heat flux condition at convective boiling of water: temperature and power-controlled experiments, in: *9th International Heat Transfer Conference, New York, 1990*.
- [52] D. Cooke, S.G. Kandlikar, Effect of open microchannel geometry on pool boiling enhancement, *Int. J. Heat Mass Transf.* 55 (4) (2012) 1004–1013, doi:[10.1016/j.ijheatmasstransfer.2011.10.010](https://doi.org/10.1016/j.ijheatmasstransfer.2011.10.010).
- [53] A. Jaikumar, S.G. Kandlikar, Enhanced pool boiling heat transfer mechanisms for selectively sintered open microchannels, *Int. J. Heat Mass Transf.* 88 (2015) 652–661, doi:[10.1016/j.ijheatmasstransfer.2015.04.100](https://doi.org/10.1016/j.ijheatmasstransfer.2015.04.100).
- [54] P.A. Raghupathi, S.G. Kandlikar, Effect of thermophysical properties of the heater substrate on critical heat flux in pool boiling, *J. Heat Transf.* 139 (11) (2017) 111502, doi:[10.1115/1.4036653](https://doi.org/10.1115/1.4036653).
- [55] S.S. Bukhari, J.Y. Vardaxoglou, W. Whittow, A metasurfaces review: definitions and applications, *Appl. Sci.* 9 (13) (2019), doi:[10.3390/app9132727](https://doi.org/10.3390/app9132727).
- [56] T. Gric, O. Hess, Chapter 5 – metasurfaces, in: T. Gric, O. Hess (Eds.), *Phenomena of Optical Metamaterials, Micro and Nano Technologies*, Elsevier, 2019, pp. 131–154, doi:[10.1016/B978-0-12-813896-0.00005-5](https://doi.org/10.1016/B978-0-12-813896-0.00005-5).
- [57] A. Lininger, A.Y. Zhu, J.-S. Park, G. Palermo, S. Chatterjee, J. Boyd, F. Capasso, G. Strangi, Optical properties of metasurfaces infiltrated with liquid crystals, *Proc. Natl. Acad. Sci.* 117 (34) (2020) 20390–20396, doi:[10.1073/pnas.2006336117](https://doi.org/10.1073/pnas.2006336117).
- [58] M. Yang, P. Sheng, Sound absorption structures: from porous media to acoustic metamaterials, *Annu. Rev. Mater. Res.* 47 (1) (2017) 83–114, doi:[10.1146/annurev-matsci-070616-124032](https://doi.org/10.1146/annurev-matsci-070616-124032).
- [59] G. Hwang, M. Kaviany, High-heat-flux distributed capillary evaporators, in: K. Vafai (Ed.), *Handbook of Porous Media*, Taylor and Francis & CRC Press, 2015, pp. 535–555, doi:[10.1201/b18614](https://doi.org/10.1201/b18614).
- [60] N.H. Afgan, L.A. Jovic, S.A. Kovalev, V.A. Lenykov, Boiling heat transfer from surfaces with porous layers, *Int. J. Heat Mass Transf.* 28 (2) (1985) 415–422, doi:[10.1016/0017-9310\(85\)90074-2](https://doi.org/10.1016/0017-9310(85)90074-2).
- [61] G.-S. Hwang, M. Kaviany, Critical heat flux in thin, uniform particle coatings, *Int. J. Heat Mass Transf.* 49 (5) (2006) 844–849, doi:[10.1016/j.ijheatmasstransfer.2005.09.020](https://doi.org/10.1016/j.ijheatmasstransfer.2005.09.020).
- [62] G. Hwang, Y. Nam, E. Fleming, P. Dussinger, Y. Ju, M. Kaviany, Multi-artery heat pipe spreader: experiment, *Int. J. Heat Mass Transf.* 53 (13) (2010) 2662–2669, doi:[10.1016/j.ijheatmasstransfer.2010.02.046](https://doi.org/10.1016/j.ijheatmasstransfer.2010.02.046).
- [63] D. Min, G. Hwang, Y. Usta, O. Cora, M. Koc, M. Kaviany, 2-D and 3-D modulated porous coatings for enhanced pool boiling, *Int. J. Heat Mass Transf.* 52 (11) (2009) 2607–2613, doi:[10.1016/j.ijheatmasstransfer.2008.12.018](https://doi.org/10.1016/j.ijheatmasstransfer.2008.12.018).
- [64] G. Hwang, E. Fleming, B. Carne, S. Sharratt, Y. Nam, P. Dussinger, Y. Ju, M. Kaviany, Multi-artery heat-pipe spreader: lateral liquid supply, *Int. J. Heat Mass Transf.* 54 (11) (2011) 2334–2340, doi:[10.1016/j.ijheatmasstransfer.2011.02.029](https://doi.org/10.1016/j.ijheatmasstransfer.2011.02.029).
- [65] T.K. Kim, Enhancement of critical heat flux in a flow channel with capillary wicking structure, Pohang University of Science and Technology, Pohang, Republic of Korea, 2022 Ph.D. thesis.
- [66] F. Nicoud, F. Ducros, Subgrid-Scale stress modelling based on the square of the velocity gradient tensor, *Flow Turbul. Combust.* 62 (1999) 183–200, doi:[10.1023/A:1009995426001](https://doi.org/10.1023/A:1009995426001).
- [67] Y. Murai, X. qun Song, T. Takagi, M. aki Ishikawa, F. Yamamoto, J. Ohta, Inverse energy cascade structure of turbulence in a bubbly flow: PIV measurement and results, *JSME Int. J. Ser. B* 43 (2) (2000) 188–196, doi:[10.1299/jsmeb.43.188](https://doi.org/10.1299/jsmeb.43.188).